

Full paper

Layer-by-layer assembly for ultrathin energy-harvesting films: Piezoelectric and triboelectric nanocomposite films



Seokmin Lee^a, Bongjun Yeom^{b,*}, Younghoon Kim^{c,*}, Jinhan Cho^{a,*}

^a Department of Chemical and Biological Engineering, Korea University, 145 Anam-ro, Seongbuk-gu, Seoul 02841, Republic of Korea

^b Department of Chemical Engineering, Hanyang University, 222 Wangsimni-ro, Seongdong-gu, Seoul 04763, Republic of Korea

^c Convergence Research Center for Solar Energy, DGIST Convergence Research Institute, 333 Techno Jungang-daero, Hyeonpung-myeon, Dalseong-gun, Daegu 42988, Republic of Korea

ARTICLE INFO

Keywords:

Layer-by-layer assembly
Piezoelectric nanoparticles
Ferroelectric nanoparticles
Piezoelectric film
Triboelectric film
Surface morphology control

ABSTRACT

Energy-harvesting devices such as piezoelectric and triboelectric nanogenerators (NGs), which can convert mechanical energy into electricity, are under development to be combined with various electronics. In particular, the rapid progress in microscale electronics such as nanorobotics or microelectromechanical devices has strongly increased the demand for ultrathin film devices. Therefore, the thickness, highly uniform structure, chemical composition, interfacial adhesion/interactions, and electrical performance of electrically active films should be carefully considered for high-performance ultrathin energy-harvesting devices. This review focuses on how layer-by-layer (LbL) assembly as a kind of thin film technology can be effectively applied to ultrathin piezoelectric and triboelectric films, and furthermore enhance device performance. First, we introduce the basics of various LbL assemblies using electrostatic, hydrogen-bonding, and covalent-bonding interactions. Then, the LbL-assembly-assisted piezoelectric and triboelectric NGs reported to date are reviewed. Finally, we briefly present perspectives on the direction of LbL assembly for the realization of various ultrathin piezoelectric and triboelectric NGs with high performance.

1. Introduction

Since the first introduction of the layer-by-layer (LbL) assembly method using cationic and anionic polyelectrolytes (PEs) in 1991–1992 by Decher et al. [1,2], this assembly method has been demonstrated to offer a high potential and versatile opportunity to prepare functional nanocomposite films with tailored film thickness, composition, and functionality on substrates of different size and shape [3–16]. Keeping pace with these notable methodological advantages, the material components used for the preparation of various functional LbL-assembled films have explosively expanded from simple insulating PEs to a variety of functional polymers, carbon materials (carbon nanotubes, graphene oxide) and inorganic nanomaterials (metal or metal-oxide-based nanoparticles, nanowires, and 2D sheets); furthermore, the complementary interactions have also varied from electrostatic interactions to covalent bonding interactions [17–36]. Based on these unique qualities, LbL-assembled organic/organic and organic/inorganic multilayer films have been widely used for the preparation of various applications such as light-emitting diodes [24,35], membranes [21], drug delivery systems [34], nonvolatile memory devices [18,25,27], electrochromic films [28], energy storage electrodes [31,35], and surface-modulated films (e.g., antireflective and superhydrophobic films) [17,19]. Furthermore, with the aid of this LbL assembly approach, it has been demonstrated that the performance of thin-film devices is strongly influenced and further enhanced by the precise control of the loading amount, the surface coverage, and the interfacial chemical species of desired functional components in addition to the type and size of organic linkers including polymer binders in the nanoscale range.

However, in spite of these notable versatility of LbL assembly, relatively little effort has been focused on the preparation of energy-harvesting nanocomposite films that can convert ambient and sporadic mechanical energy into electricity. In particular, given that piezoelectricity- or triboelectricity-based energy-harvesting nanogenerators (NGs) require electrically active nanocomposite films with tailored electrical transfer, controlled surface morphology, and large area, the application of LbL assembly to energy-harvesting NGs can strongly contribute to the enhancement of energy-harvesting performance/stability and to a better understanding of the energy-harvesting mechanism, preparation of ultrathin film

devices, solution-based manufacturing process, and mass production. Additionally, with rapid progress in various portable electronic devices and microscale devices, increased interest in ultrathin energy-harvesting films can considerably stimulate the use of LbL assembly. Excellent reviews exist in the area of functional nanocomposite films based on LbL assembly; however, few studies on energy-harvesting NGs using the LbL approach have been reported to date. In this review, we introduce the basics of LbL assembly and demonstrate that the LbL assembly can be effectively applied to piezoelectric and triboelectric NGs. Furthermore, we demonstrate that electric output performances of piezoelectric and triboelectric NGs can be significantly controlled and enhanced by LbL assembly.

2. Basics of layer-by-layer assembly

LbL-assembled nanocomposite films are prepared through repetitive and alternating adsorption/washing processes of different components allowing complementary attractive interactions such as electrostatic interactions, hydrogen bonding, and covalent bonding (Fig. 1a) [1–36]. The loading number of LbL-assembled components is significantly influenced by the deposition time, solution concentration, degree of complementary interactions, and deposition layer number. In particular, in the case of electrostatic LbL assembly performed in aqueous media, additional assembly conditions such as ionic strength (or ionic salt concentration) and/or solution pH are required for the control of the adsorbed amount per layer [2,8,14,17]. These phenomena are universally applicable to almost all the components with electrostatically charged species ranging from polyelectrolytes (PEs) to nanoparticles in aqueous media.

For example, in the case of strong PEs with fixed charge density such as poly(sodium styrenesulfonate) (PSS) carrying sulfonate groups (SO_3^-) or poly(diallyldimethylammonium chloride) (PDADMAC) carrying ammonium groups (Fig. 1b) [8], the electrostatic repulsion between the same charged groups causes PE chains to be adsorbed onto the substrates with flat and stiff chain conformation, resulting in low surface coverage and layer thickness of a few angstroms (Å). However, the addition of ionic salt such as NaCl to PE solutions induces the decrease in electrostatic repulsion between inter- and/or intramolecular groups by counter ions of ionic salts, and the chain

* Corresponding authors.

E-mail addresses: byeom@hanyang.ac.kr (B. Yeom), younghoon.kim@dgist.ac.kr (Y. Kim), jinhan71@korea.ac.kr (J. Cho).

conformation of PE is changed from flat to entangled and/or coiled chains by counter ions of ionic salts, which increases the thickness of the PE layer adsorbed onto the substrate. Therefore, the total film thickness of strong PE multilayers such as (PSS/PDADMAC)_n multilayers is controlled by the ionic strength in addition to the PE concentration, the deposition time, and the bilayer number (n).

Different from strong PEs, the charge density of PEs such as anionic poly(acrylic acid) (PAA) carrying carboxylate ion (COO⁻) groups or cationic poly(allylamine hydrochloride) (PAH) with protonated amine (NH₃⁺) groups is greatly affected by the solution pH (Fig. 1b) [6,37,38]. The PEs with these pH-dependent charge densities are called weak PEs, and weak PEs such as PAA and PAH have two different forms that allow electrostatic bonding (by COO⁻ for PAA and by NH₃⁺ for PAH) and hydrogen bonding (by the carboxylic acid group (COOH) for PAA and by NH₂ for PAH) at a moderate solution pH. With increasing pH of weak PE solutions, the uncharged COOH groups of PAA are changed into negatively charged COO⁻ groups, whereas the cationic NH₃⁺ groups of PAH are converted into neutral amine (NH₂) groups. Using these properties, a large amount of electrostatically and hydrogen-bonded weak PE chains per layer can be incorporated into multilayer films under some specific pH conditions, and the acid treatment to the formed films can generate porous films as a result of rearrangement of electrostatically charged and hydrogen-bonded PE chains. More specifically, the (PAH/PAA)_n multilayers can form the thickest film at a pH of 7.5 for PAH and a pH of 3.5 for PAA. However, the subsequent acidic treatment (pH ≤ 2.5) of these films generates a highly porous surface morphology because the partial electrostatic bonding between the COO⁻ groups of PAA and the NH₃⁺ group of PAH within the multilayers is fully dissociated and rearranged by the formation of additional COOH groups of PAA at low pH [37]. These porous films can be used as a mold for the preparation of functional films with hierarchical structures (specifically, a mold for triboelectric PDMS films with nanoscale and microscale bumpy structures).

Furthermore, electrostatically charged metal or metal oxide nanoparticles (NPs) can be LbL assembled with oppositely charged polymers in aqueous media using the same deposition methods. However, the control over the ionic strength and the pH of NP solutions for increasing the loading number of NPs adsorbed per layer is challenging relative to that of weak PE solutions because the decrease in electrostatic repulsion between the same charged NPs can easily cause NP agglomeration and/or sedimentation. Additionally, the use of electrostatically charged NPs with a dilute solution concentration and unfavorable qualities (i.e., a broad size distribution or low crystallinity of NPs) tends to restrict the formation of densely packed NP arrays (the packing density of a charged NP layer is < 30%) [39,40] and the desired functionalities of resultant LbL multilayers, respectively. Furthermore, the electrostatic LbL-assembled NP films are generally unsuitable for capacitor-type devices such as piezoelectric NGs with a metal-insulator-metal (MIM) structure due to the evolution of undesirable leakage current arising from residual moisture.

As an alternative, many studies have recently focused on the preparation of (hydrophobic metal or metal oxide NP/polymer)_n multilayers using complementary covalent-bonding interactions in organic media [41,42]. Although various metal or metal oxide NPs with high quality (i.e., with uniform size and high crystallinity) have been synthesized using hydrophobic stabilizers with carboxylic acid, amine, or ammonium moieties (e.g., oleic acid (OA), palmitic acid (PA), or tetrabutylammonium (TOA)) in organic media, the conventional LbL assembly of hydrophobic NPs in conjunction with polymers has generally required a phase transfer step from nonpolar to aqueous media using

selective and limited ligands that facilitate weak electrostatic and/or hydrogen-bonding interactions. However, more recently, it has been reported that OA-, PA-, and TOA-stabilized metal or metal oxide NPs can be directly LbL assembled with NH₂-functionalized organics in organic media due to the higher affinity of the bare surface of metal or metal oxide with NH₂ moieties (Fig. 1c) [30,32,36,43–45]. These findings clearly imply that the well-defined hydrophobic NPs ranging from metal to binary or perovskite-type NPs can be directly LbL-assembled with various NH₂-functionalized polymers in organic media exhibiting high packing density and desired functionalities of NPs; furthermore, the formed nanocomposite multilayers can be effectively applied to various capacitor-type devices such as piezoelectric devices requiring low leakage current levels.

3. Piezoelectric nanogenerators using layer-by-layer assembly

In the case of capacitor-type piezoelectric nanogenerators (PENGs) composed of metal electrodes (i.e., top and bottom electrodes) and a piezoelectric layer, a variety of perovskite-type materials such as barium titanate (BaTiO₃, BTO) [46–49], potassium niobate (KNbO₃) [50,51], or zinc stannate (ZnSnO₃) [52,53] have been used as electrically active films because of their excellent piezoelectricity and ferroelectricity that originate from noncentrosymmetric properties, associated with how much transition metal cations distorted in the perovskite lattice. However, the use of sub-10 nm perovskite NPs for ultrathin energy-harvesting films is severely restricted because bulky organic ligands bound to the surface of NPs result in poor processability (such as that associated with phase separation and/or the segregation of NPs within polymeric matrices) and consequently obstruct the formation of stable and homogeneous films. These phenomena also hinder the formation of an experimental consensus on the critical size at which the size-dependent piezoelectricity/ferroelectricity of the perovskite NPs is suppressed [54]. Notably, most studies of perovskite NP-based energy-harvesting devices reported to date have focused on the use of large NPs (> 100 nm) [46–49]. However, considering that the surface of perovskite NPs has a high affinity with amine (NH₂) groups, these sub-10 nm perovskite NPs can be LbL assembled with NH₂-functionalized organic linkers, resulting in (perovskite NP/NH₂-organic linker)_n multilayer films with piezoelectric properties [44,45]. Additionally, the piezoelectric performance of the formed ultrathin multilayers can be easily and precisely controlled by the bilayer number (n), the adsorbed number of NPs, and the type of organic linkers and external applied force during the measurements, will be discussed in detail in 3.2.2. section.

3.1. Ferroelectric nanomaterials for piezoelectric nanogenerators

3.1.1. Ferroelectric polymers

Preceding a detailed discussion of LbL-assembled piezoelectric NGs, we introduce organic and inorganic ferroelectric materials for piezoelectric NGs. First, ferroelectric polymers, such as poly(vinylidene fluoride) (PVDF), have been widely used in piezoelectric NGs because of their high flexibility, ease of solution processing, spontaneous polarization, high dielectric constant, and strong piezoelectricity. More specifically, PVDF with fluorine-terminated functional groups, which is well known as a semicrystalline ferroelectric polymer, shows different crystalline phases according to its lattice structure and chain conformation. Among its various crystalline phases, the β-phase of PVDF exhibits the highest piezoelectric coefficient of -29 pm V^{-1} , originating from the strongest dipole moment of 2.10 D perpendicular to the β-phase chain conformation (Fig. 2a and b) [55,56]. Therefore, the β-phase PVDF have been the most widely used as an active layer for the preparation of piezoelectric NGs with high electric output performance [57–59]. Additionally, these PVDF polymers can be easily solution processed to fabricate a piezoelectric active layer with the desired forms (i.e., thin films and wires) because of their spontaneous dissolution in various polar solvents such as methyl-ethyl-ketone (MEK) and dimethylformamide (DMF). After the formation of an amorphous PVDF film, the β-phase PVDF with higher ferroelectricity can be obtained through an additional thermal annealing process (near the Curie temperature of PVDF) and electrical poling process.

Based on these phenomena, various PVDF-based copolymers such as poly(vinylidene fluoride-co-hexafluoropropene) (P(VDF-HFP)), poly(vinylidene fluoride-co-trifluoroethylene) (P(VDF-TrFE)), poly(vinylidene fluoride-co-chloride trifluoroethylene) (P(VDF-CTFE)), and poly(vinylidene fluoride-trifluoroethylene-chlorotrifluoroethylene) (P(VDF-TrFE-CFE)) have also been employed to further improve the ferroelectric and piezoelectric properties (Fig. 2c) [58,59]. Considering that the dipole moments of PVDF are generated only in the direction perpendicular to the polymer chains and that their ferroelectricity is therefore highly dependent on chain conformation, the PVDF-based copolymers with the all-*trans* chain conformations can significantly enhance the dipole moments, resulting in improved ferroelectricity and piezoelectricity.

However, these PVDF-based copolymers still exhibit relatively low thermal, mechanical and dielectric properties relative to those of inorganic ferroelectric and piezoelectric materials. For resolving these drawbacks, inorganic piezoelectric nanomaterials (> 100 nm in size) such as perovskite BaTiO₃ have been generally incorporated into PVDF-based copolymer matrices for high-performance piezoelectric device applications. Additionally, for the preparation of active layers of piezoelectric NGs, simple blending solutions composed of PVDF-based copolymers and bulky piezoelectric nanomaterials have been deposited onto the electrodes using the spin-coating or doctor blade-coating method, which generally produces a relatively thick film over a few μm thickness (Fig. 2d and e) [46–49]. However, these conventional methodologies encounter challenges in inducing a homogeneous and uniform distribution and controlling the loading amount of inorganic piezoelectric nanomaterials within the PVDF-based copolymer matrix. In most cases, thermodynamically unfavorable interfacial interaction between inorganic nanomaterials and polymer matrix causes severe NP agglomerations and/or phase separation, which can have a fatal effect on the uniformity/consistency of device performance and furthermore is inappropriate for ultrathin-film device applications [60]. Given by the fact that PVDF-based copolymers are highly dispersed in polar solvent as mentioned above, these

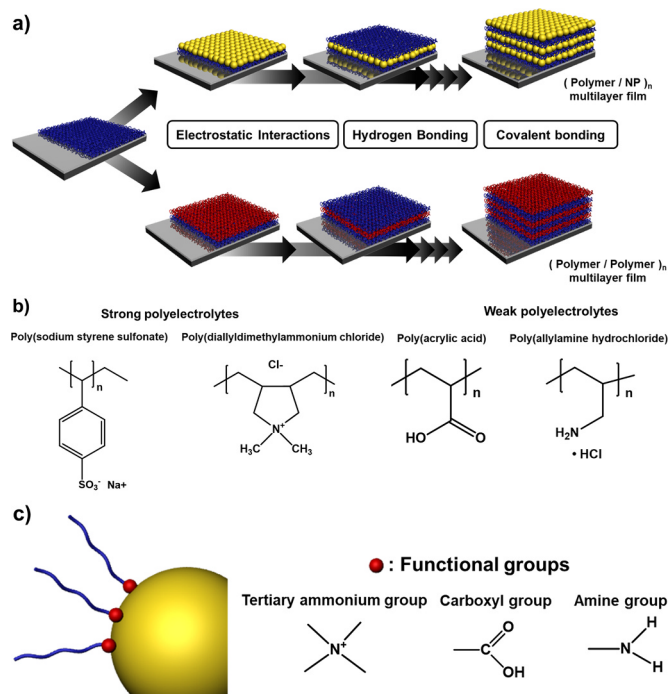


Fig. 1. a) Schematic overview of LbL assembly using electrostatic interactions, hydrogen bonding, and covalent bonding. b) Molecular structures of strong electrolytes (PSS and PDADMAC) and weak electrolytes (PAA and PAH). c) Affinity between metal or metal oxide nanoparticles and various functional groups in organic media.

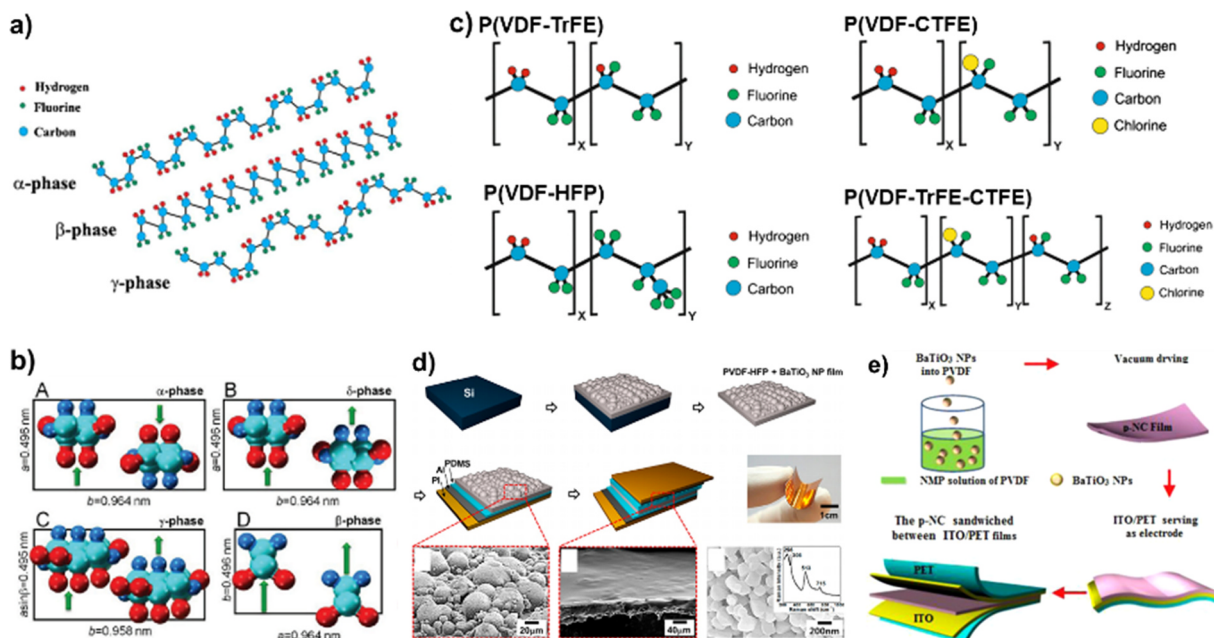


Fig. 2. a) Schematic representation of the chain conformation for the α , β , and γ phases of PVDF [55]. b) Unit cells of PVDF crystals viewed along the c -axes. Red, cyan, and blue spheres represent fluorine, carbon, and hydrogen atoms, respectively. The projections of dipole directions are indicated by green arrows [56]. Reproduced with permission from ACS (2012). c) Schematic representation of PVDF-based copolymers [55]. Reproduced with permission from Elsevier B.V. (2014). d) Schematic illustration and photo image of the nanogenerator composed of PDMS-covered BTO-P(VDF-HFP). Bottom shows the SEM images of BTO-P(VDF-HFP) composite film, PDMS-covered BTO-P(VDF-HFP) composite film, and BTO NPs, respectively [47]. Reproduced with permission from ACS (2014). e) The detailed fabrication procedure of flexible piezoelectric nanocomposites composed of PVDF and BTO NPs [48]. Reproduced with permission from Elsevier B.V. (2015). (For interpretation of the references to color in this figure legend, the reader is referred to the web version of this article.)

polymers are expected to be alternatively LbL-assembled with the BTO NPs in nonpolar solvent due to the orthogonal solvent effects. Therefore, we expect as a prospective approach that the PVDF copolymer/BTO NP thin films could be fabricated with precisely controlled film thickness and amount of piezoelectric nanomaterials in polymer matrix.

3.1.2. Ferroelectric perovskite oxides

As mentioned above, perovskite oxides with an ABO_3 ($A = Ba, Sr, Pb, \text{etc.}$; $B = Ti, Zr, \text{etc.}$) lattice formula, such as $PbTiO_3$, $BaTiO_3$ (BTO), $SrTiO_3$ (STO) and $Pb(Zr,Ti)_2O_7$ (PZT), have attracted considerable attention due to their excellent ferroelectric and piezoelectric properties, which are dominated by how much the B-site cations

surrounded by A-site cations and oxygen in the perovskite lattice structure are distorted [61–64]. Ferroelectric perovskite oxides have been recognized as promising piezoelectric materials for energy harvesting because of their electrically and mechanically induced spontaneous polarizations, leading to high device performance with or without an electrical poling process [49,53,65–69]. For practical applications of piezoelectric NGs, perovskite oxide nanomaterials have generally been prepared using three different processes as follows: first, the perovskite oxides are fabricated using vacuum deposition methods [70,71], such as pulsed laser deposition (PLD) (Fig. 3a and b) or radio frequency (RF) sputtering. Second, the oxide perovskite materials, such as nanoparticles (NPs), nanowires, and nanotubes, are prepared in the form of ceramic films or powders

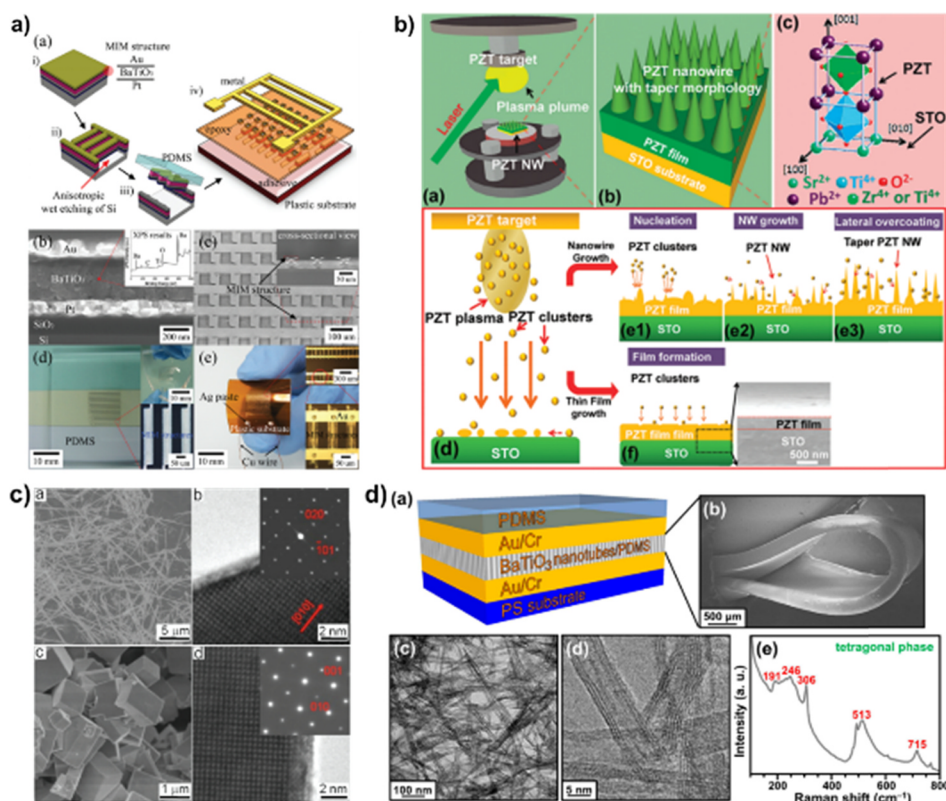


Fig. 3. a) Schematic illustration of the fabrication process of flexible BTO nanogenerator on plastic substrates fabricated using RF magnetron sputtering, standard microfabrication and soft lithographic printing techniques [70]. Reproduced with permission from ACS (2010). b) Schematic illustration of fabrication process of PZT nanowire arrays on a STO substrate via PLD technique [71]. Reproduced with permission from ACS (2012). c) SEM and TEM images of $NaNbO_3$ nanowires and nanocubes synthesized using sol-gel-derived solution process [72]. Reproduced with permission from ACS (2011). d) Scheme of the as-developed nanogenerators fabricated using BTO nanotubes, with the SEM image of the BTO nanotubes/PDMS composite and TEM images, Raman spectrum of the synthesized BTO nanotubes [73]. Reproduced with permission from ACS (2012).

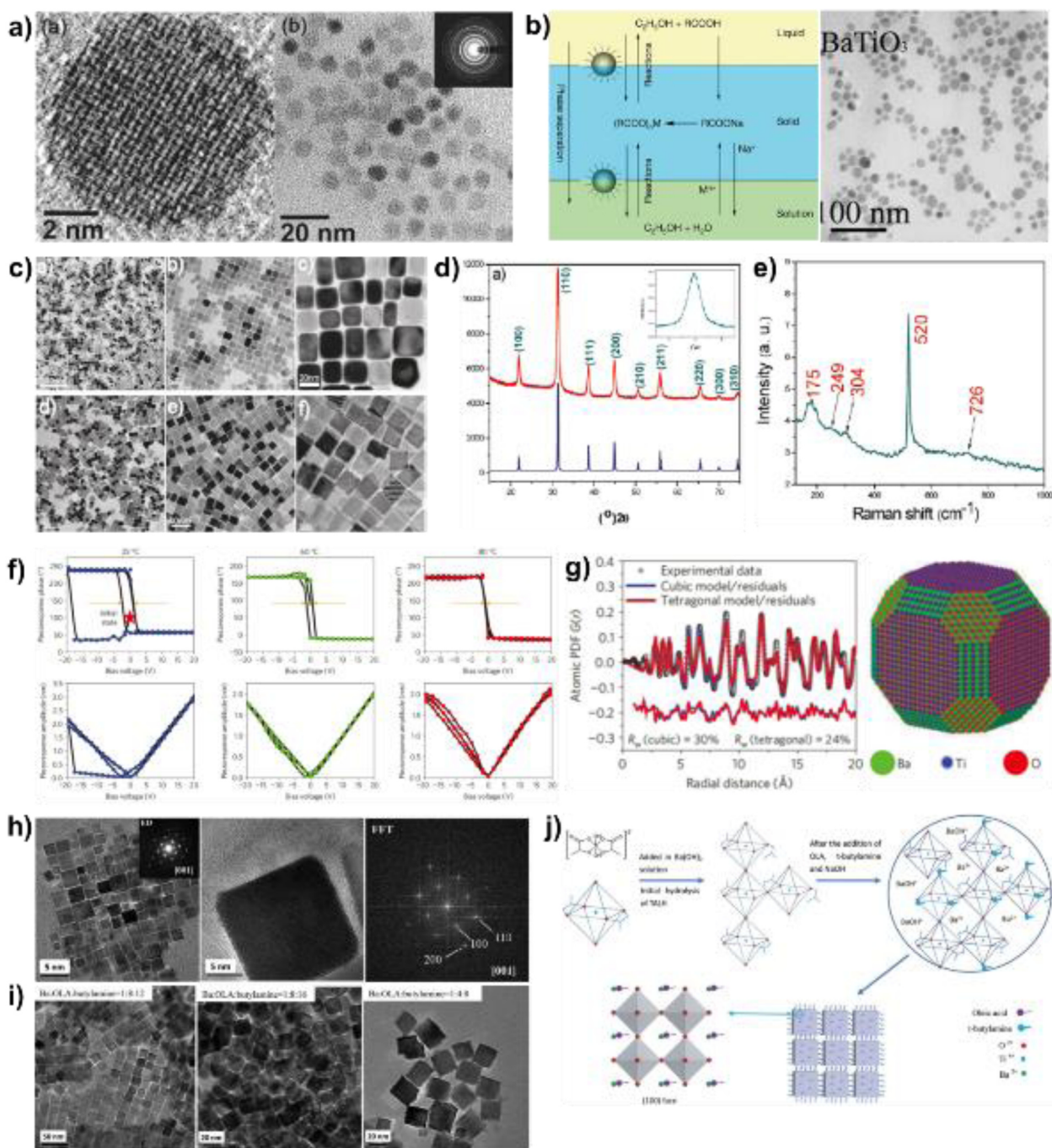


Fig. 4. a) TEM micrographs of a high-resolution lattice image of an individual 8 nm diameter BTO NP and an ensemble of discrete BTO NPs. Inset: Selected area electron diffraction (SAED) pattern [75]. Reproduced with permission from ACS (2001). b) Schematic illustration of liquid-solid-solution (LSS) phase transfer synthetic strategy for the synthesis of BTO NPs and TEM image of the as-synthesized BTO NPs. Inset: Colloidal dispersion of BTO NPs in cyclohexane [76]. Reproduced with permission from Springer Nature (2005) c) TEM images of monolayers of cubelike (top) and cubic (bottom) BTO NPs. d) XRD pattern and e) Raman spectrum of the 22 nm cubelike BTO NPs. Reprinted with permission from reference [82]. Reproduced with permission from ACS (2010). f) Piezoresponse phase (top) and amplitude (bottom) for a single 10 nm BTO nanocube measured by PFM at 25, 60, and 80 °C, respectively. g) Atomic PDF and model structures for 8 nm-BTO nanocubes [54]. Reproduced with permission from Springer Nature (2012). h) TEM images of the particles synthesized at 200 °C in 1 mol L⁻¹ NaOH with a molar ratio of Ba : OLA : butylamine = 1 : 8 : 8 for 72 h. i) TEM images of the particles synthesized at 200 °C in 1 mol L⁻¹ NaOH with the molar ratios of Ba : OLA : butylamine = 1 : 8 : 12, 1 : 8 : 16 and 1 : 4 : 8 for 72 h. j) Schematic illustration of a possible mechanism for the development of BTO nanocubes [83]. Reproduced with permission from Royal Society of Chemistry (2012).

via sol-gel methods (Fig. 3c and d) [53,72–74]. Finally, the oxide perovskites with nanocrystal forms are synthesized via thermal decomposition, hot injection, or hydro- and solvothermal methods, producing the desired crystal size in the range from a few to tens of nanometers and a stable dispersion in organic solvent. These solution-dispersible perovskite NPs can be effectively applied to produce flexible, miniaturized and ultrathin film piezoelectric NG devices using solution processes such as LbL assembly. Therefore, we introduce a variety of synthetic approaches for ferroelectric perovskite oxide NPs reported to date in this section.

Murray et al. reported that spherical BTO NPs with diameters ranging from 6 to 12 nm could be synthesized via an injection-hydrolysis method using alkoxide-based bimetallic precursors and oleic acid stabilizers. The formed NPs exhibited a stable dispersion

in nonpolar solvents such as hexane or toluene with a narrow size distribution (Fig. 4a) [75]. This initial study opened up possibilities for the synthetic routes of size- and shape-controlled perovskite oxide NPs with high crystallinity. Li et al. reported a synthetic approach using chemical reactions at the interfaces among the different phases for the preparation of various perovskite oxide NPs including BTO and STO perovskite NPs (Fig. 4b) [76]. The resulting BTO NPs with a diameter of approximately 17 nm showed a tetragonal crystal structure as confirmed by high-resolution transmission electron microscopy (HR-TEM) and X-ray diffraction (XRD) measurements. Furthermore, the synthesis and characterization of perovskite oxides in the form of colloidal nanocrystals have been intensively studied using various nanocrystal synthetic chemistry for providing chemical-composition-tunable and size-tunable properties and high crystallinity [77–81].

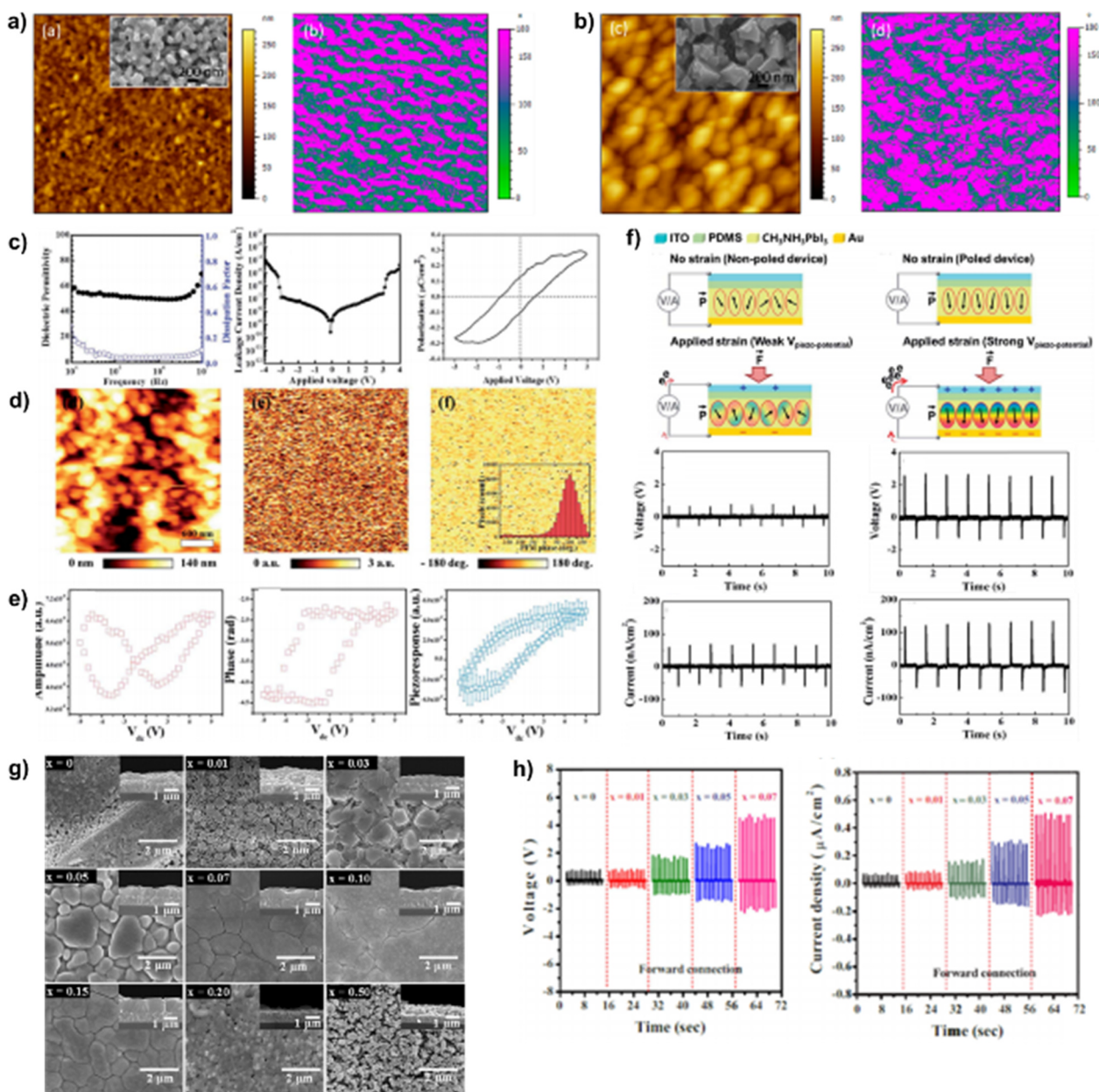


Fig. 5. Topographic and out-of-plane PFM-phase image of MAPbI₃ films a) with small crystals and b) with large crystals. Image size is $8 \times 8 \mu\text{m}^2$. PFM phase image is in false color. The insets show SEM images of the corresponding samples [87]. Reproduced with permission from ACS (2015). c) Dielectric permittivity and dissipation factor, leakage current density vs. applied voltage, and P - E hysteresis loop of the 500 nm-thick MAPbI₃ films, respectively. d) PFM topography, amplitude, and phase images of the MAPbI₃ films recorded at scan rate of 0.5 Hz, respectively. The image size is $3 \times 3 \text{ mm}^2$. e) Piezo amplitude, piezo phase, and piezoresponse hysteresis loop of the MAPbI₃ films, respectively. f) The power generation mechanisms and output performance of MAPbI₃ piezoelectric thin film generators under non-poled (left) and poled (right) conditions, respectively [90]. Reprinted with permission from Royal Society of Chemistry (2016). g) SEM surface images; insets show cross-sectional images for different incorporated concentrations of Fe²⁺ in MAPb_{1-x}Fe_xI₃ thin films. h) Output voltage and current density of MAPb_{1-x}Fe_xI₃ ($0 \leq x \leq 0.07$) piezoelectric generators measured by forward connection [91]. Reproduced with permission from Elsevier B.V (2018). (For interpretation of the references to color in this figure legend, the reader is referred to the web version of this article.)

In addition to spherical-type NPs, high-quality and monodisperse BTO NPs with cube-like shapes of approximately 20 nm size were introduced by Caruntu et al. [82]. These BTO NPs were synthesized using oleic acid ligands via thermal decomposition of metal complex precursors under hydrothermal conditions, and they were well dispersed in nonpolar media due to the hydrophobic oleic acid ligands bound to the surface of NPs. The resulting BTO NPs exhibit the results of distorted Ti⁴⁺ ions in pseudocubic perovskite lattices, which contribute to ferroelectric and piezoelectric properties as confirmed by XRD and Raman spectra (Fig. 4c–e). Ramesh et al. observed the ferroelectric and piezoelectric behaviors of isolated single BTO NPs at room temperature [54]. They also reported that the polarization switching of sub-10 nm BTO NPs was driven by direct electrical measurements, and their switching behavior disappeared below a critical size ranging from 5 to 10 nm as confirmed by atomic pair distribution function (PDF) and piezoresponse force microscopy (PFM) studies. Although the 10 nm BTO NPs exhibited a piezoelectric coefficient of 1.55 pm V^{-1} , which is much lower than that of bulk BTO (75 pm V^{-1}), these results imply that the sub-10 nm BTO NPs preserve the piezoelectric properties (Fig. 4f and g).

Furthermore, Dang et al., reported the crystal growth kinetics of BTO NPs that were synthesized using bis(ammonium lactate) titanium dihydroxide (TALH), oleic acid and tert-butylamine under solvothermal conditions [83]. TALH is a Ti⁴⁺ precursor, six-

coordinated with the octahedral oxygen groups in the form of TiO₆ octahedra, facilitating hydrolysis and condensation. The size and morphology of BTO NPs are determined by the solution concentration of oleic acid used as ligands, and then cube-shaped BTO NPs are formed by the addition of tert-butylamine suppressing the further growth of [TiO₆] building blocks during the synthesis. The resulting BTO NPs showed cubic morphologies, uniform size distribution, high crystallinity and favorable dispersion in organic media. They also demonstrated that other perovskite oxide NPs such as STO and Ba_xSr_{1-x}TiO₃ could be successfully synthesized using the modified synthetic routes based on the abovementioned formation mechanism of cube-shaped BTO NPs [84–86].

3.1.3. Organic-inorganic lead halide perovskites

Organic-inorganic lead halide perovskites, with an APbX₃ (A = methylammonium (MA), formadimium (FA)/X = I, Br, Cl) lattice formula, have been frequently used as a photoactive material in optoelectronic applications such as solar cells and light-emitting diodes (LEDs). Recently, it has been confirmed by PFM studies [87] that lead halide perovskites feature ferroelectric polarization originating from the rotations of the BX₆ octahedron cage and dipolar A-site cations inside the perovskite lattice structures

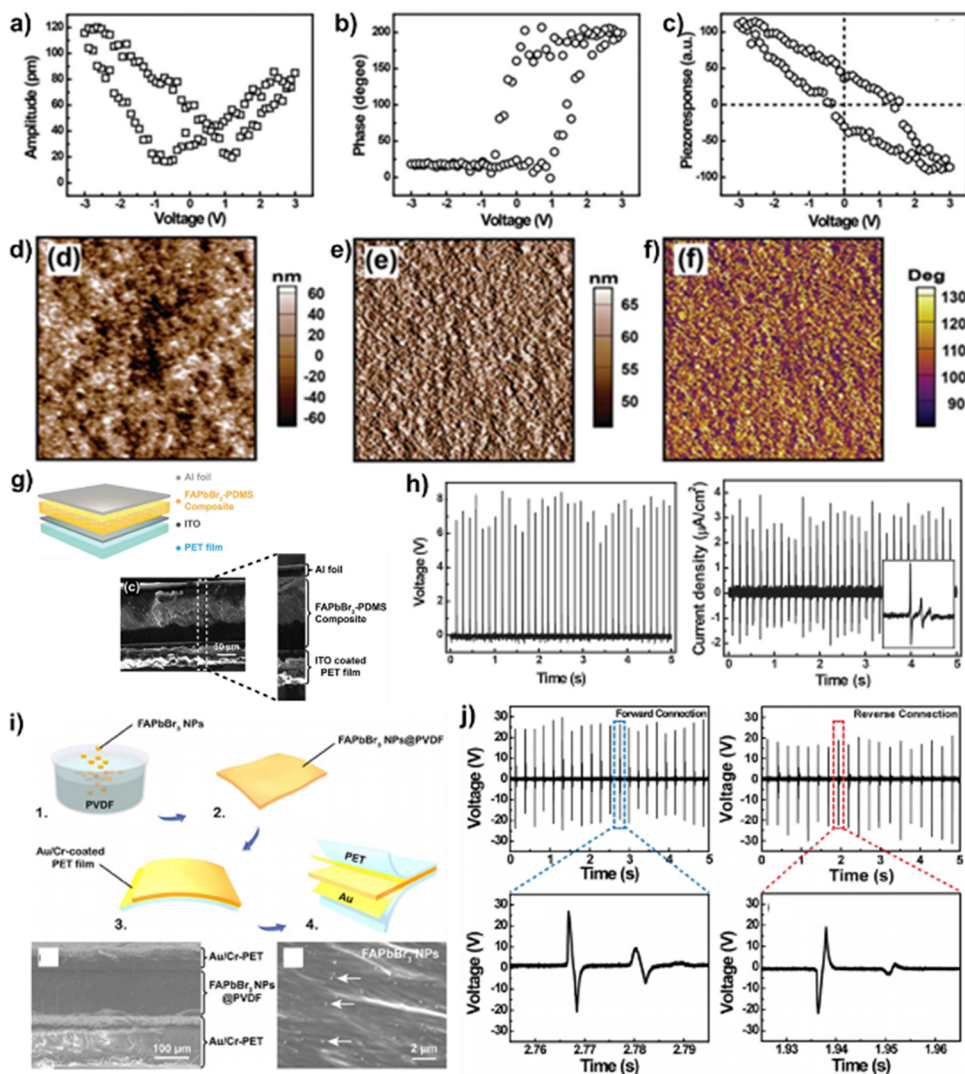


Fig. 6. a) Amplitude “butterfly” loop ($A(E)$). b) Phase hysteresis loop ($\varphi(E)$) obtained with a DC voltage of 1 V. c) The piezoresponse hysteresis loop, $PR(E)$, which is calculated and plotted using the equation $PR(E) = A(E) \cos(\varphi(E))$. d) Topography, e) amplitude, and f) phase images of the FAPbBr₃ NPs, respectively. The size for the images is $20 \times 20 \mu\text{m}^2$. g) Schematic diagram and cross-sectional SEM image of piezoelectric nanogenerator composed of FAPbBr₃-PDMS composite. h) Output voltage and current density from FAPbBr₃ NPs composite nanogenerator induced by periodically vertical compression [92]. Reproduced with permission from Wiley (2016). i) The detailed fabrication procedure of composite nanogenerator based on FAPbBr₃ NPs @ PVDF. Bottom shows the cross-sectional SEM image of the nanogenerator and the magnified cross-sectional SEM image of FAPbBr₃ NPs, which are randomly distributed inside the PVDF polymer. j) Piezoelectric output voltage of the FAPbBr₃ NPs@PVDF composite-based nanogenerator in the forward connection (left) and the reverse connection (right) [93]. Reproduced with permission from Elsevier B.V (2017).

(Fig. 5a and b) [87–89]. Based on these properties, organic-inorganic lead halide perovskites have been successfully used as a piezoelectric layer in the piezoelectric NGs with metal-insulator-metal (MIM) device architectures, driven by external mechanical forces. Yoon et al. reported that solution-processed MAPbI₃ perovskite thin films have ferroelectric and piezoelectric properties using the measurements of Curie temperature, dielectric constant, and polarization–electric field (P – E) curve; consequently, these films can be used as an active layer for piezoelectric NGs [90]. Additionally, the piezoelectric performance of MAPbI₃ perovskite NGs is significantly enhanced through electric poling process, resulting in an output voltage of 2.7 V and a current density of 140 nA cm^{-2} . They also reported that in the case of incorporating Fe²⁺ cations into the perovskite structure, the piezoelectric coefficient of MAPbI₃ perovskites could be increased up to 17.6 pm V^{-1} as a result of the improved surface morphologies and crystallinities of perovskites [91]. In particular, when the concentration of Fe²⁺ was increased ($x = 0.07$), the phase transition temperature of MAPb_{1-x}Fe_xI₃ decreased by approximately 45 °C, which improved the dielectric and ferroelectric properties. As a result, the output voltage and current density of piezoelectric NGs based on the Fe²⁺-incorporated MAPbI₃ perovskite thin films were increased to approximately 7.29 V and $0.88 \text{ }\mu\text{A cm}^{-2}$, respectively, after electric poling (Fig. 5g and h). Zheng et al. also demonstrated that the FAPbBr₃ NP-polydimethylsiloxane (PDMS) nanocomposite films sandwiched between flexible ITO electrode and aluminum (Al) foils exhibit high piezoelectric performance with an output voltage of 8.5 V and a current density of $3.8 \text{ }\mu\text{A cm}^{-2}$ under a periodic compressive force of 0.5 MPa after the electric poling process [92]. In this case, the FAPbBr₃ NPs had ferroelectric properties with a high piezoelectric coefficient (d_{33}) of 25 pm V^{-1} (Fig. 6a and b). Furthermore, when ferroelectric PVDF was used instead of the PDMS matrix [93], the device performance (including an output voltage of 30 V and a current density of $6.2 \text{ }\mu\text{A cm}^{-2}$) of FAPbBr₃-based piezoelectric NGs was significantly enhanced due to the higher piezoelectric coefficient of the PVDF polymer matrix ($\sim 29 \text{ pm V}^{-1}$) (Fig. 6i and j). However, as mentioned earlier, the preparation of FAPbBr₃ NP-PDMS nanocomposite films using a simple blending process can cause NP aggregation and/or phase segregation within the formed nanocomposites.

3.2. Layer-by-layer assembled ferroelectric and piezoelectric applications

BTO NPs have been recognized as one of the most promising perovskite-type

ferroelectric NPs for use in piezoelectric NGs due to their strong piezoelectric properties and lead-free chemical composition. In most cases, the BTO NPs with size of a few hundred nanometers are blended with polymers via solution mixing and mechanical stirring for the preparation of BTO/polymer nanocomposite films [49,94,95]. These conventional approaches are inappropriate for preparing ultrathin film devices ($< 200 \text{ nm}$) because of the formation of relatively thick BaTiO₃/polymer films ($> 10 \text{ }\mu\text{m}$) in addition to NP aggregation and/or phase segregation. To resolve these critical issues, two important factors must be satisfied: First, the successful synthesis of high-quality BTO NPs with approximately 10 nm size and high colloidal stability in organic media is required. Second, the unique LBL assembly, which can bridge the two different interfaces between hydrophobic BTO NPs and polymers in organic media, is required for the preparation of nanocomposite films with the high loading amount of BTO NPs and the controlled thickness. In this section, we review LBL-assembled piezoelectric films based on hydrophobic BTO NPs with 8 and 13 nm sizes.

3.2.1. Layer-by-layer assembled BaTiO₃ nanoparticle films with ferroelectric properties

Cho et al., for the first time, reported that the oleic acid-stabilized BTO NPs with sub-10 nm size could be LBL-assembled with (NH₂)-functionalized polyamidoamine dendrimers via a unique ligand-addition LBL assembly process based on the covalent-bonding interaction between the Ti⁴⁺ cations within BTO NPs and the NH₂ groups of dendrimers (Fig. 7a) [44]. The LBL growth mechanism of (BTO NP/dendrimer)_n nanocomposite thin films as a function of bilayer number (n) was demonstrated using Fourier transform infrared (FTIR) and X-ray photoelectron spectroscopy (XPS). These results indicated that the NH₂ moieties of dendrimers are additionally adsorbed onto the Ti⁴⁺ cation sites existing on the surface of BTO NPs without the removal of the original surface ligands (i.e., oleic acid) bound to the Ba²⁺ cations. The adsorbed amount of 8 nm BTO NPs in the nanocomposite thin films was quantitatively investigated via a quartz crystal microgravimetry (QCM) measurement and was calculated to have a number density of $5.12 \times 10^{11} \text{ cm}^{-2}$ using the Sauerbrey equation with the frequency change measured from QCM [96]. In addition, the thickness of nanocomposite thin films linearly increased from 50 to 204 nm as a function of bilayer number, showing the extremely smooth surface morphologies (Fig. 7b–e).

The (BTO NP/dendrimer)_n nanocomposite thin films showed typical ferroelectric properties with reversible spontaneous polarization, confirmed by a polarization–electric

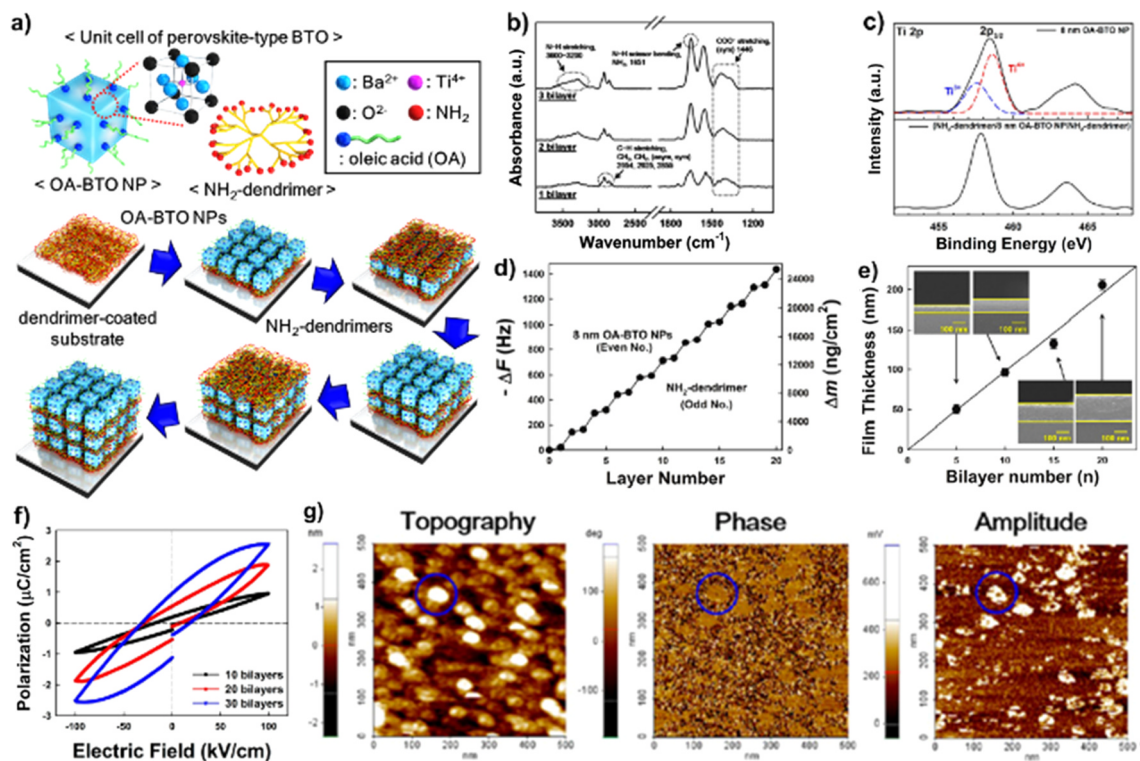


Fig. 7. a) Schematic diagram of the (perovskite NP/ NH_2 -functionalized organic linker) $_n$ multilayer films. b) ATR-FT-IR spectra of the (NH_2 -dendrimer/OA-BTO NP) $_n = 1,2,3$ multilayers as a function of the bilayer number (n). c) XPS spectra of Ti 2p collected from the OA-BTO NPs and NH_2 -dendrimer-encapsulated films [i.e., (NH_2 -dendrimer/OA-BTO NP/ NH_2 -dendrimer) multilayer]. d) Frequency and mass change of the NH_2 -dendrimer/OA-BTO NPs multilayers as a function of the layer number. e) Total film thicknesses of the (NH_2 -dendrimer/OA-BTO NP) $_n = 5,10,15,20$ multilayers measured from the cross-sectional SEM images. f) P - E curves for the (NH_2 -dendrimer/OA-BTO NP) $_n = 10,20,30$ multilayers. g) Topographic, phase, and amplitude images from the DC-EFM for the OA-BTO NPs on a Pt-coated substrate [44]. Reproduced with permission from ACS (2014).

field (P - E) measurement. The polarization switching of respective BTO NPs was confirmed from the phase and amplitude images measured by dynamic-contact electrostatic force microscopy (DC-EFM). In addition, the ferroelectric properties of LbL-assembled nanocomposite thin films were controlled according to the bilayer numbers (i.e., film thickness) related to the loading amount of BTO NPs. Although it was reported that the ferroelectricity of BTO NPs with a size of less than 5–10 nm disappeared due to the influence of depolarizing field generated within BTO NPs [54], the nanocomposite films composed of 8 nm BTO NPs still exhibited ferroelectric properties occurring from the

tetragonality of distorted Ti^{4+} cations within the BTO lattice. Therefore, these results clearly indicate that the sub-10 nm BTO NPs can be effectively used as a ferroelectric material in nanoscale device applications (Fig. 7f and g).

3.2.2. Layer-by-layer assembled BaTiO_3 nanoparticle films for piezoelectric NGs

It was reported by Cho et al. that LbL-assembled (13 nm BTO NP/polymer) $_n$ ferroelectric nanocomposite thin films could be successfully used in a piezoresponsive

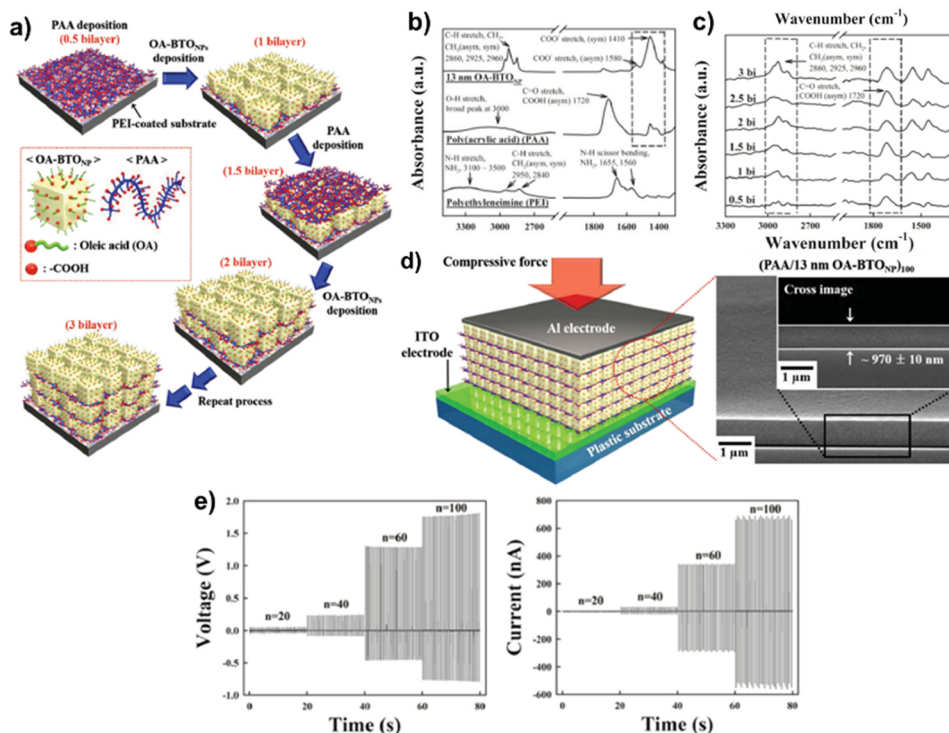


Fig. 8. a) A schematic illustration of the LbL growth of a PAA/OA-BTO NP multilayer. b) FT-IR spectra of 13 nm OA-BTO NP, PAA, and PEI, respectively. c) FT-IR spectra of the (PAA/13 nm OA-BTO NP) $_n$ multilayers as a function of the number of bilayers. d) A schematic illustration of a piezoelectric nanogenerator based on a (PAA/OA-BTO NP) $_n$ multilayer. e) The output voltage and current of the multilayered piezoelectric nanogenerators as a function of the number of bilayers (n) [45]. Reproduced with permission from Wiley (2014).

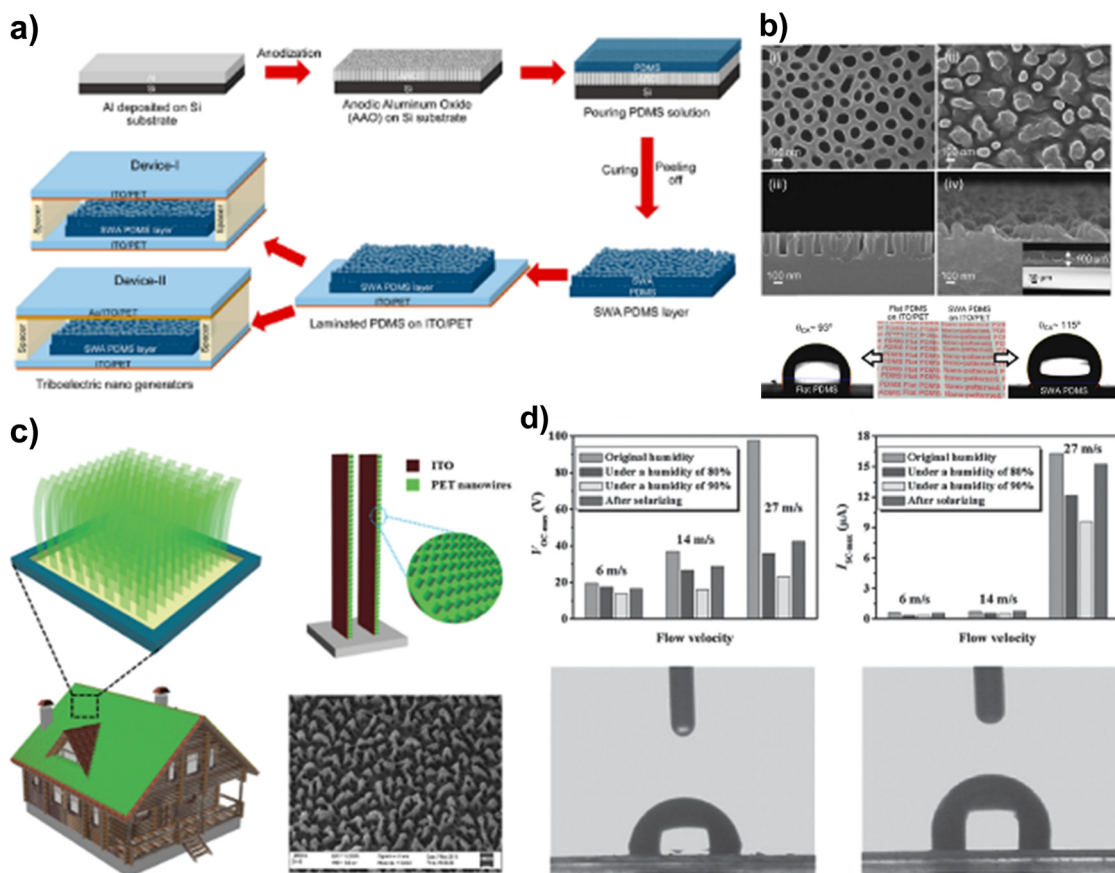


Fig. 9. (a) Schematics for the fabrication of the TENG device with the SWA PDMS replicated by the AAO template. (b) SEM images of the AAO template (i and iii) and the SWA PDMS (ii and iv), and photographs indicating water contact angles on flat and SWA PDMS layer [118]. Reproduced with permission from ACS (2015). (c) Schematic illustrations of the lawn structured TENG, which is consisted of PET nanowire array. (d) Influence of the humidity on the open-circuit voltage and short-circuit current of the lawn structured TENG, and water contact angles on ITO (left) and PET nanowire array (right) [124]. Reproduced with permission from Wiley (2016).

active layer in piezoelectric NGs for energy harvesting. In their study, the nanocomposite films were prepared using ligand addition-induced LbL assembly between oleic acid-stabilized BTO NPs and PAA in nonpolar solvent [45]. In this case, the existing metal ions on the surface of BTO NPs are coordinated with the carboxylic acid groups of PAA polymers. As confirmed by FT-IR spectroscopy, the Ti^{4+} cations on the surface of BTO NPs are covalently bound to COO^- functional groups of PAA polymers due to their higher affinity without the removal of pristine oleic acid ligands. Furthermore, they reported that the piezoelectric performance (i.e., output voltage and current) of LbL-assembled $(BTO\ NP/polymer)_n$ nanocomposite films could be significantly increased by increasing the bilayer number and/or the compressive force without any electrical poling process. The highest output performance was obtained from the approximately $1\ \mu m$ -thick nanocomposite device with an output voltage and current of 1.8 V and 700 nA, respectively. These results imply that the LbL-assembly approach can be used as an effective tool for developing and designing ultrathin piezoelectric NGs using a variety of perovskite-type ferroelectric nanomaterials including BTO NPs (Fig. 8).

4. Triboelectric nanogenerators using layer-by-layer assembly

Triboelectric nanogenerators (TENGs) represent another important application among LbL-assembled energy-harvesting devices. TENGs can generate electricity from irregular frictional contacts between different triboelectric surfaces with tailored surface

functionalities and morphologies [97–105]. Therefore, there have been significant efforts to implement TENGs into the wearable smart devices as sustainable power sources without involving conventional batteries [106–109]. In this embodiment, larger differences in electron affinity of two contact surfaces and larger surface areas can generate higher electrical outputs under the application of the same degree of external forces. In the case of TENGs with Al electrodes and poly(dimethylsiloxane) (PDMS) films, various types of nanostructures, such as self-assembled nanoparticles [110] and etched block copolymers [99], are introduced on the triboelectric surfaces to provide protuberant topologies at the nanoscale for the purpose of high surface area and polarity differences. However, in relatively high-humidity environments, their electric outputs rapidly deteriorate by loss of triboelectric surface charges, which can be a critical issue in practical applications. Nguyen et al. reported that TENGs composed of Al electrode and pyramidal shape-patterned PDMS showed an increase in charge generation of more than 20% under a relative humidity (RH) of 10% relative to 90% [111,112]. Therefore, the prevention of water skin layers on the triboelectric surfaces is a key requirement for better performance of TENGs in highly humid conditions.

4.1. Triboelectric nanogenerators for high humidity resistance

To resolve the aforementioned issue, several studies have adapted super-hydrophobic surfaces (water contact angle $> 150^\circ$) in the preparation of TENGs. These

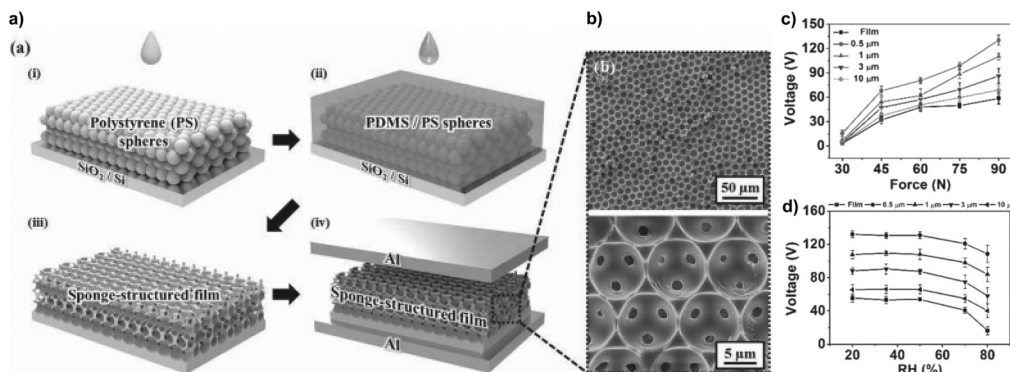


Fig. 10. (a) A schematic illustration for the fabrication process of sponge structure-based TENG (STNG) and (b) FE-SEM images of sponge-structured PDMS film. Output voltage of the FTNG and STNGs (0.5, 1, 3, and 10 μm) under various (c) compressive force and (d) relative humidity [102]. Reproduced with permission from Wiley (2014).

surfaces, which exhibit a low surface energy and large surface area arising from hierarchical micro- and nanostructures, effectively disrupt the formation of water droplets and water skin layers on top of the triboelectric surfaces. Liu et al. reported that protuberant surfaces with micro and nanostructures can effectively reduce wetting area by trapping air bubbles between rough features [113,114]. Moreover, when water vapor begins to condense under highly humid conditions, condensates form in distinct droplets on the hydrophobic surfaces that can be easily removed rather than forming liquid films [115]. For these reasons, many studies have investigated the fabrication of TENGs with superhydrophobic surfaces by utilization of a variety of surface structures, such as micro- or nanoarrays [116–126], porous sponges [102,127–129], and hierarchical structures [130–135].

The nanopillar array is one of the widely used structures in TENGs as it presents a high surface area with hydrophobic properties (ref nano array). Dudem et al. reported sub-wavelength-architecture (SWA) PDMS prepared by using nanoporous anodic aluminum oxide (AAO) template as a replica mold (Fig. 9a) [118]. Preparation of the AAO template is relatively simple and cost-effective and can be used to make a PDMS array with nanopillars of ≈ 100 nm diameter. The surface of SWA PDMS exhibited enhanced

hydrophobicity ($\theta_{CA} \approx 115^\circ$) relative to a flat PDMS surface ($\theta_{CA} \approx 93^\circ$) (Fig. 9b), and the TENGs built with SWA PDMS produced electrical outputs of 3.8 V and $0.8 \mu\text{A cm}^{-2}$ under a compressive force of 3 N. Zhang et al. reported that wind-energy-driven TENGs consisting of a polyethylene terephthalate (PET) nanowire array fabricated via reactive ion etching (RIE) (Fig. 9c) [124]. They demonstrated that the TENGs could self-regenerate their performance after exposure to high-humidity conditions (RH 90%) by inclusion of hydrophobic surfaces that can effectively suppress the presence of moisture at interfaces (Fig. 9d). This advanced enabled TENGs to operate even in outdoor environments such as on rooftops.

Porous sponge structured film also have been frequently used as triboelectric film because of its high surface to volume ratio, compressibility, and hydrophobicity. Lee et al. proposed a triboelectric hydrophobic sponge structure-based TENG (STNG) which is composed of inverse opal-structured PDMS film [102]. Polystyrene sphere based opal with face-centered cubic structure was prepared by convective evaporation, then PDMS solution infiltrated into the structure followed by curing. The inverse opal-structured PDMS film is then obtained after removal of PS spheres, and fabricated into TENG. The author conducted nanoindentation measurements, and demonstrated that a sponge-

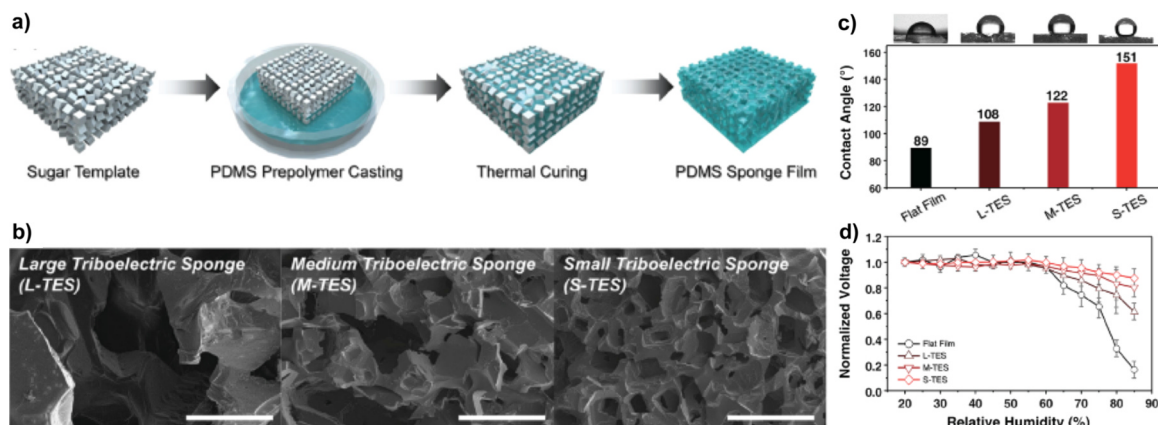


Fig. 11. (a) Schematic illustration of the fabrication procedure of the porous PDMS sponge using sugar particles (b) Morphologies of three types of triboelectric sponges (TES) using SEM. All of the scale bars (white) shown in the figures are 500 μm . (c) Static water contact angle on the TES and flat film with optical images of water droplets (d) Humidity dependency of the normalized output voltage of the TESs and flat film with a wide range of relative humidity from 20% to 85% [127]. Reproduced with permission from Wiley (2016).

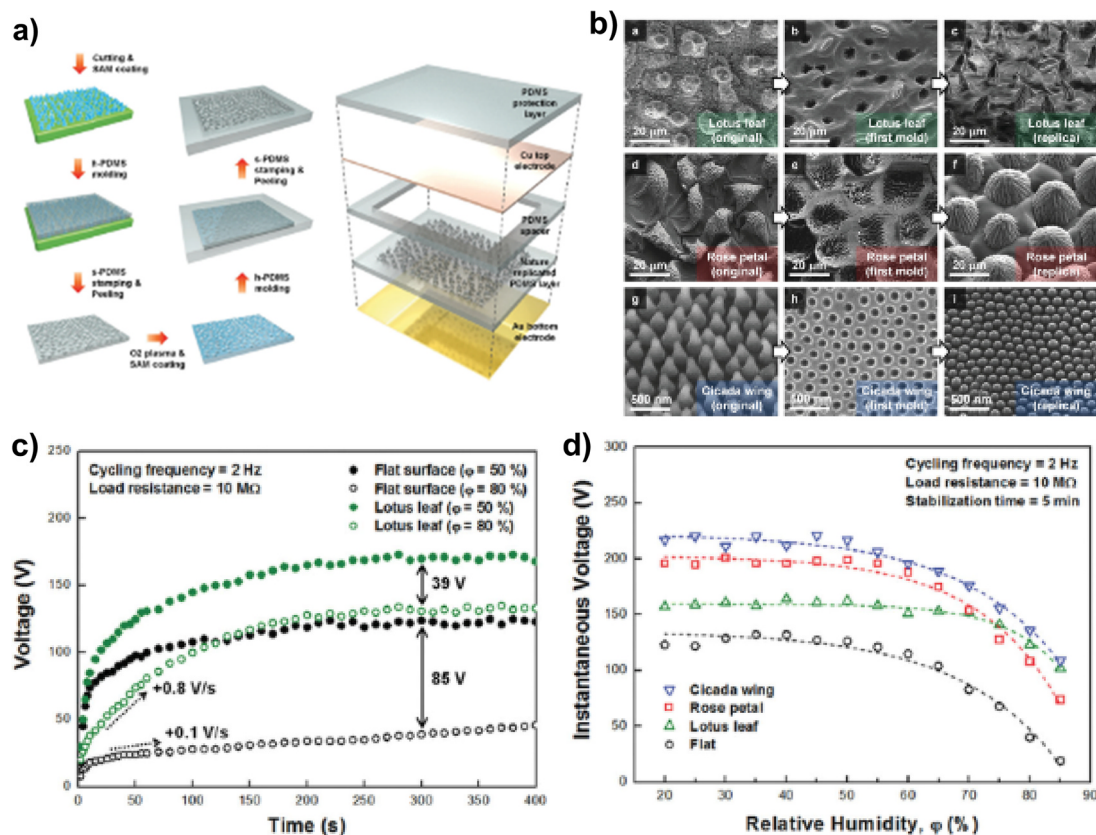


Fig. 12. (a) Schematics describing the fabrication process of the replica-molding method. (b) Results of the replica-molding process (c) Voltage–time characteristics of TENGs with the interface structures of the flat film (black) and lotus leaf (green) at a relative humidity of 50% (filled) and 80% (empty). (d) Humidity effects upon instantaneous voltage for TENGs with the interface structures of the flat, lotus leaf, rose flower, and cicada wing [133]. Reproduced with permission from Wiley (2014). (For interpretation of the references to color in this figure legend, the reader is referred to the web version of this article.)

structured PDMS film had 30% decreased elastic modulus compare to bulk film, which implies that the sponge structure possesses higher compressibility. Thus, when compressive forces are applied on the sponge structure, it becomes thinner than a bulk film, inducing the higher capacitance change. Another advantage of the triboelectric sponge

mentioned by the author is that the inner pores which do not directly contact with an electrode also play a role in additional charge generation. For the humidity resistant, voltage output of STNG showed higher electrical output performance than flat film based TENG, because of the hydrophobicity originated from upward force generated by

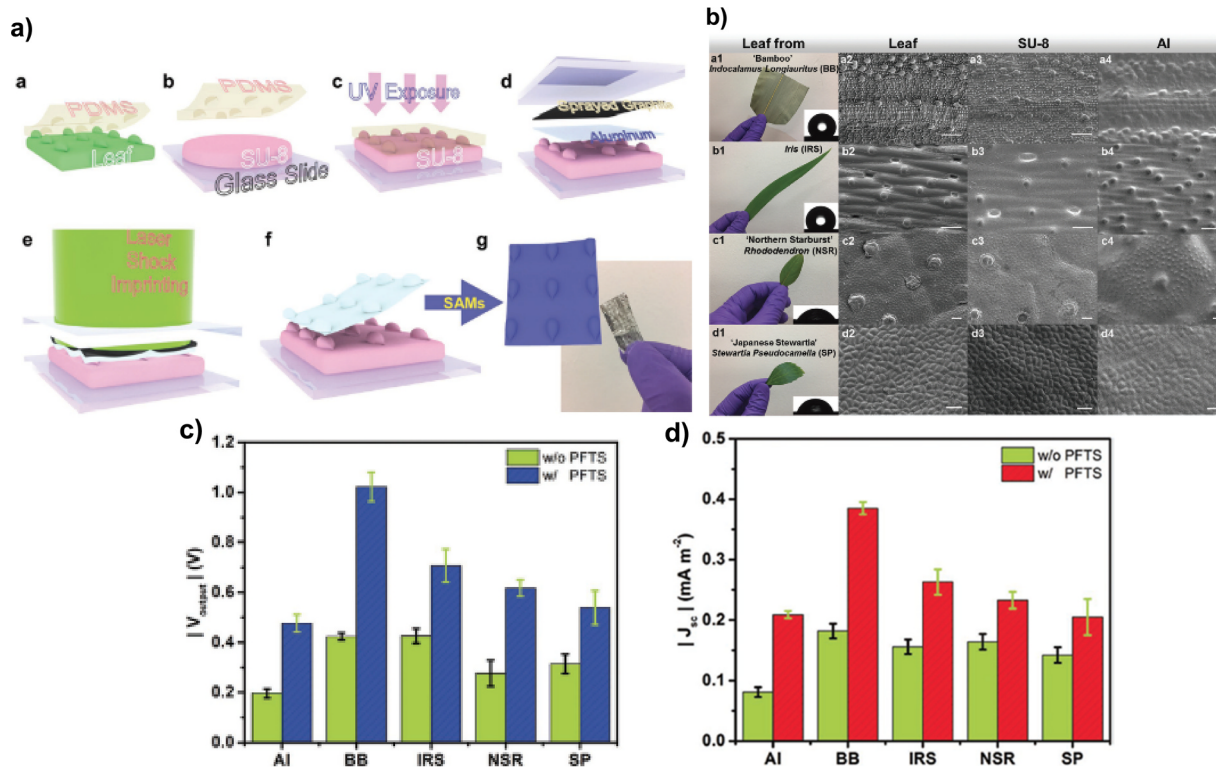


Fig. 13. (a) Schematic illustration of a) substrate transfer from leaf to PDMS, b) SU-8 spin coated on a glass slide, c) UV flood exposure of SU-8, d) pre-setup of LSI, e) LSI process, f) the free-standing LSI/Al foil peeled from SU-8 mold, and g) SAMs-coated water-TENG (lower-right: a digital photo of the final product). (b) Leaves from (a1) Bamboo (BB), (b1) Iris (IRS), (c1) Northern Starburst (NSR), and (d1) Japanese Stewartia (SP). Their respective contact angle measurement (inset) and SEM images of original leaves are presented from (a2) to (d2), respective SEM images of SU-8 shown from (a3) to (d3), and respective SEM images of LSI/Al listed from (a4) to (d4). (Scale bar: 80 μm). (c) Absolute voltage output comparison among non-LSI-processed and different LSI-processed leaves (green and nonshaded) and corresponding devices with PFTS coated (blue and shaded) (d) Absolute short-circuit current density comparison among non-LSI-processed and different LSI-processed (green and nonshaded) and corresponding devices with PFTS coated (red and shaded) [134]. Reproduced with permission from Wiley (2018). (For interpretation of the references to color in this figure legend, the reader is referred to the web version of this article.)

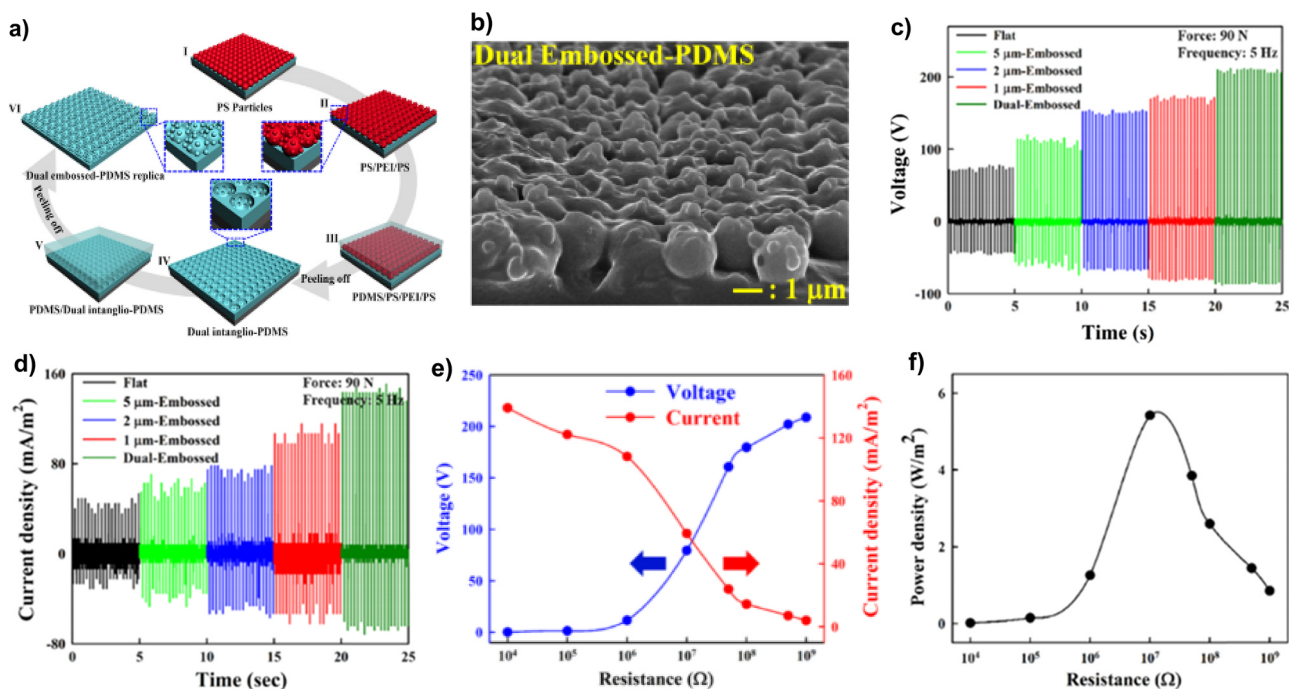


Fig. 14. (a) Schematic showing the preparation of dual-embossed-PDMS films. (b) FE-SEM image of dual-embossed-PDMS films. (c) Total output voltages and (d) current densities of a flat TENG, 1 μm - and 2 μm -embossed-FTENGs and a dual embossed-FTENG. (e) Dependence of the peak voltage and peak current density on external load resistance under the compressive force of 90 N. (f) Dependence of the instantaneous power output on external load resistance under the compressive force of 90 N [138]. Reproduced with permission from Elsevier B.V (2016).

the air inside the pores (Fig. 10).

Kim et al. reported a triboelectric sponge fabricated from a commercially available cube sugar as a template, exhibiting superhydrophobicity [127]. The sponge structure was fabricated via PDMS casting on sugar cube followed by sugar template removal. Pore sizes of the sponge were controlled by using different sizes of sugar particles, 1500, 500, and 300 μm , respectively. The largest electrical outputs were exhibited from TENG with pore size of 300 μm because the amounts of triboelectrically induced charges increases with the contact surface area. Further, hydrophobicity of the films were examined by measuring water contact angle on its surfaces, and the sponge with 300 μm -sized pore exhibited superhydrophobicity with approximately 151° of static water contact angle originated from over-hang-like structure (re-entrant profile) on the surface (Fig. 11).

Seol et al. prepared nature-replicated nano/micro structures through multi-replica process with lotus leaves, rose petals, and cicada wings [133]. In nature, those surfaces present superhydrophobic properties due to their nano-in-micro hierarchical bumps. The authors integrated such unique features into TENGs. In particular, energy generation from TENGs with cicada wing replica films was enhanced 3 times relative to TENGs with flat surface films. Furthermore, the lotus leaf replica showed efficient suppression of the humidity presenting the lowest level of 85% from the original output performance. The enhancements are attributed to the hierarchical morphologies in the bump structures with high aspect ratios (Fig. 12).

Recently, Jin et al. demonstrated water-drop-energy-harvesting TENGs with 3D biomimetic hierarchical metal surfaces fabricated by a laser-shock imprinting (LSI) method. As described in the case of conventional TENGs based on the contact-separation mode, the control of surfaces to be hydrophobic is the most critical factor since water droplets must be removed to induce electron flows. The laser-shock imprinting process induces the superplastic state of metal using short laser pulses so that the metal can deform conformably and fit to the surface of a nanoscale mold [134]. Various types of leaves, such as bamboo and iris, with nano/microhierarchical surface morphologies were used to fabricate molds for the LSI process. The biomimetic structures were replicated on the surface of Al foils. In addition, Al surfaces with pristine water contact angle of 80° were treated with fluorinated silane to produce hydrophobicity measured as 105° of the water contact angle (Fig. 13).

Although such rough surfaces can be fabricated by the use of natural templates, the sizes and shapes of surface structures transferred to the PDMS replicas are essentially dependent of those of the natural templates. Therefore, such limits in the control of microstructures stimulate the development of general and facile fabrication routes for the preparation of TENGs with dual-size topologies at the nanoscale and microscale. Along with such efforts in the fabrication of high-performance TENGs with humidity resistance, LbL assemblies were used in the realization of hierarchical surface topologies. These LbL-assembled TENGs can significantly enhance the charge generation by their high surface area while effectively obstructing the formation of water droplets.

4.2. Force-assembled triboelectric nanogenerators with hierarchical surface morphology

Large-area production of TENGs with hydrophobic surfaces remains challenging. The reproducibility of hierarchical micro and nanostructures and the mechanical durability of such structures are the most important concerns in the large-area fabrication of TENGs. In this regard, the force-assembly method for colloidal monolayer fabrication has advantages over conventional methods [136]. This method uses mechanical rubbing of colloids between two rubbery materials, such as PDMS, for the preparation of hexagonally packed colloidal monolayers. In principle, the mechanical rubbing process can be applied to any substrate size; a substrate of wafer size was demonstrated [137]. Various sizes of intaglio and embossed microstructures can be prepared over large areas with high reproducibility.

On the basis of these features, force-assembled TENGs (FTENGs) were fabricated and showed strong electrical performance, mechanical durability, and humidity resistance [138]. Polystyrene (PS) colloids in dried powder form with a diameter of 1, 2, or 5 μm were used to form a hexagonally packed array on a PDMS substrate through a mechanical rubbing process. The array was used as a first mold to replicate intaglio-structured PDMS with micropores. The prepared intaglio-PDMS film was then used as second mold to produce an embossed microstructured PDMS replica film. Moreover, an additional layer of PS nanocolloids was introduced onto the hexagonally packed PS microsize colloidal monolayer to impart a dual scale of roughness on the microscale and nanoscale. In detail, a cationic poly(ethylene imine) (PEI) layer was deposited on a force-assembled array of 2 μm PS colloids, resulting in a positively charged PEI-coated microscale PS colloidal monolayer. Then, anionic PS colloids with 600 nm size were adsorbed over the PEI-coated microsize PS colloidal monolayer via electrostatic self-assembly. The resultant film contained a dual length scale of roughness arising from the microscale and nanoscale PS colloids. Such colloidal films with dual roughness scales can serve as templates for intaglio-PDMS films and can be further used to produce dual embossed-PDMS films by a subsequent replication process (Fig. 14a).

The open-circuit voltage and current density of a dual-embossed-FTENG were 207 V and $14.1 \mu\text{A cm}^{-2}$ under a compressive force of 90 N. The power density of dual-embossed-FTENG was examined with external loads, and the instantaneous power density reached a maximum of 5.42 W m^{-2} with 10 M Ω external load resistance (Fig. 14c–f).

The dual-embossed PDMS films present superhydrophobic surface properties originating from its unique hierarchical structures with dual length scales that consist of nanosized protuberances on embossed microstructures. Static water contact angles of flat, embossed, and dual-embossed PDMS films were increased from 106° to 125° to 136° respectively (Fig. 15a). The dual-embossed FTENG exhibited humidity resistance. The output voltage was 174 V at 80% RH, representing only 16% loss relative to the output voltage at 20% RH. In contrast, the flat TENG lost 85% of the output voltage in the same test. The dual-embossed PDMS films exhibited significant mechanical stability during

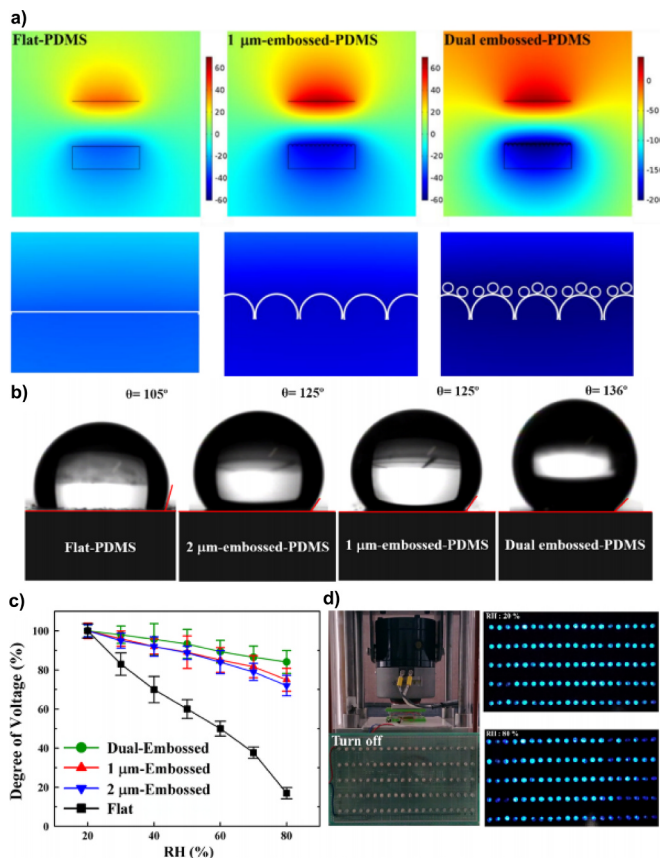


Fig. 15. (a) Analytical (or color-coded) results showing triboelectric potential differences of flat, 1 μm -embossed and dual-embossed-PDMS films under the same compressive force, as simulated using the COMSOL multiphysics software. In this case, dual embossed-PDMS exhibited the largest potential differences. (b) Water contact angles on flat-TENG, 1 μm and 2 μm -embossed and dual-embossed-PDMS films. (c) The output voltages of flat TENG, 1 μm and 2 μm -embossed and dual-embossed-FTENGs as functions of RH. In these cases, a 22 cycled compressive force of 90 N was used for the triboelectric measurements. The respective data points were the average values obtained from 100 cycles. (d) The use of electrical energy generated by the dual-embossed-FTENGs to operate 100 LEDs at 20% and 80% RH [138]. Reproduced with permission from Elsevier B.V. (2016). (For interpretation of the references to color in this figure legend, the reader is referred to the web version of this article.)

18,000 cycles of compressive loadings with 5 Hz frequency, attributed to the incorporated hierarchical structures at dual length scales (Fig. 15b).

In addition, analytical simulations were conducted with the COMSOL Multiphysics package to investigate how the dual-sized morphology affects tribo-induced electric potentials. All top electrodes were assigned with triboelectric charge density of $\pm 32.3 \mu\text{C/m}^2$ (Fig. 15a). In comparison of the flat and the embossed morphologies, the dual-embossed morphology shows remarkable enhancement of triboelectric potential, suggesting that much higher charge density can be generated when the surface contains nanoscale and microscale hierarchical structures.

4.3. Electrostatic layer-by-layer assembly-induced triboelectric NGs with high and stable electric output

LbL-assembled films associated with weak polyelectrolytes have capabilities for manipulations of their nanoscale and microscale structures by control of molecular interactions. Rubner et al. reported that LbL-assembled films consisting of weak polyelectrolytes (PEs) could be reversibly transformed from smooth surface films to highly porous films with a significant degree of roughness [37,139]. Poly(allylamine hydrochloride) (PAH) and poly(acrylic acid) (PAA) were used for demonstrations of such transformation. The pore size and surface morphologies can be controllable to a great degree depending on the film compositions, pH conditions, and salt concentrations. Such versatile fabrication methods involving LbL-assembled films could be a potential approach to realize superhydrophobic surfaces for improvements of TENG performance in humid conditions (Fig. 16a).

The sizes and the morphology of pores in LbL-assembled films can be systematically controlled by changing the PE solution concentration used in the LbL assembly process [140]. It has been observed that the overall pore size decreases with decreasing PAA solution concentration. Notably, unique morphologies with nanoscale pores embedded in the microsize pores could be observed (Fig. 16c). The evolution of such hierarchical structures is attributed to the excessive amount of PAA chains within the film, which

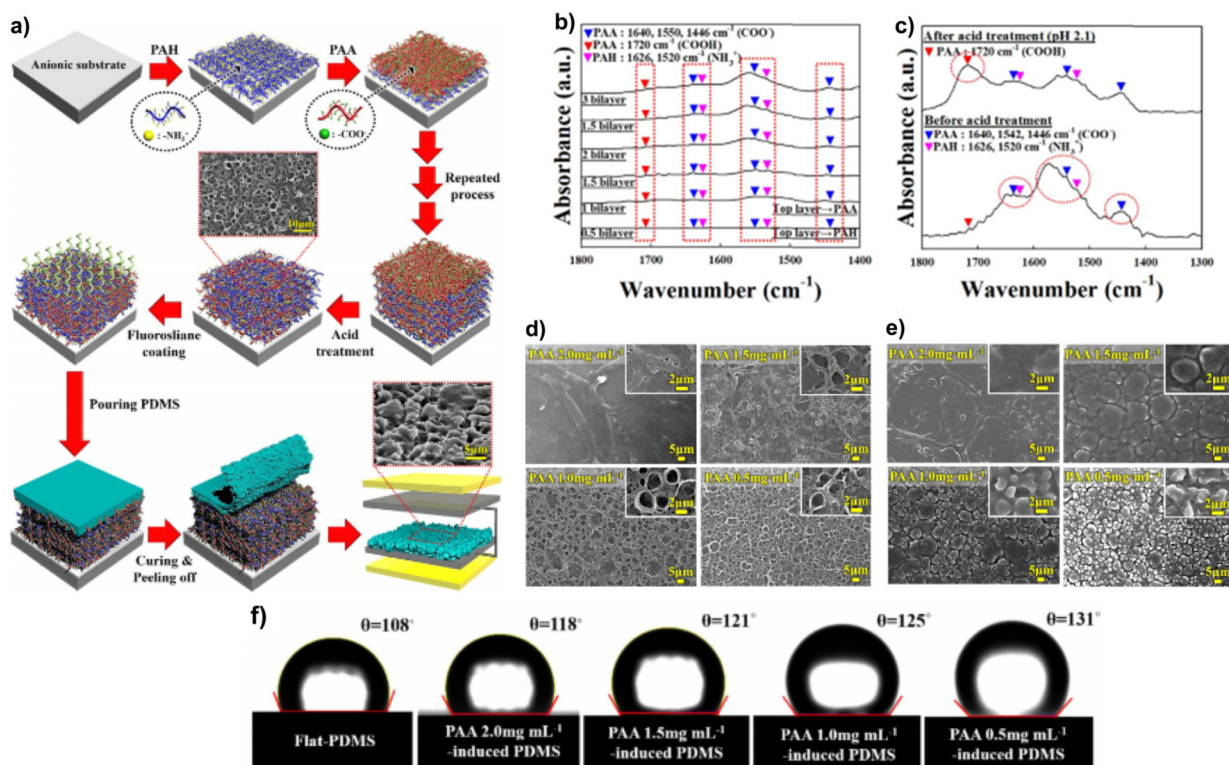


Fig. 16. (a) Schematic for the preparation of triboelectric PDMS films with hierarchically embossed structures using porous PE-multilayered templates. (b) ATR-FTIR spectra of [PAH/PAA]_n multilayers as a function of the bilayer number. (c) ATR-FTIR spectra of pristine and acid-treated PAH/PAA multilayers during 15 min. (d) Top-view FE-SEM images of porous [PAH/PAA]₂₀ multilayer templates prepared from four different solution concentrations of PAA (2, 1.5, 1.0, and 0.5 mg mL⁻¹). In this case, the solution concentration of PAH and the pH value for the acid treatment were fixed at 1.5 mg mL⁻¹ and 2.1 mg mL⁻¹, respectively. (e) Top-view FE-SEM images of the embossed PDMS films replicated from the [PAH/PAA]₂₀ templates with four different porosities. (f) Static contact angles of water drops on flat, [1.5 mg mL⁻¹ PAH/ 2.0 mg mL⁻¹ PAA]₂₀, [1.5 mg mL⁻¹ PAH/1.5 mg mL⁻¹ PAA]₂₀, [1.5 mg mL⁻¹ PAH/1.0 mg mL⁻¹ PAA]₂₀, [1.5 mg mL⁻¹ PAH/0.5 mg mL⁻¹ PAA]₂₀ template-molded PDMS films. All the LbL-assembled multilayer templates were treated with a pH 2.1 aqueous solution [140]. Reproduced with permission from Elsevier B.V (2018).

increases the degree of rearrangements and inhibits the formation of nanosized pores. The porous LbL-assembled films were further used as molding templates for the fabrications of PDMS films with nanoscale/microscale hierarchical surface structures. As shown in Fig. 16d, a PDMS replica of [1.5 mg mL⁻¹ PAH/0.5 mg mL⁻¹ PAA]₂₀ films presents hierarchical morphologies with a nano/microembossed structure with a static water contact angle of 131° (Fig. 16e). The contact angle is increased over that of flat PDMS due to development of Cassie state of wetting by the presence of trapped air at the film-air interfaces. Therefore, it can be estimated that PDMS surfaces with such hydrophobicity can efficiently suppress water layer formation, potentially increasing the electrical output of TENGs in humid conditions.

The electrical output of a TENG with a flat film and LbL-TENGs was measured under a compressive force of 10–90 N at a 5 Hz frequency. The open-circuit voltage and short-circuit current density of the flat TENG were 81 V and 8.9 μA cm⁻², respectively, and those of the LbL-TENG showed significant improvements of outputs of 242 V and 16.2 μA cm⁻², respectively. The increased electric outputs could be explained by the hierarchical morphology with larger surface area and higher compressibility than that of flat PDMS film. A compressible structure with a large surface area not only can induce more capacitance change but also results in larger electrostatic induction area [102]. Under humid environments at 80% relative humidity, the LbL-TENGs retained their output performances up to 80% with a V_{oc} of 194 V and I_{sc} of 12.6 μA cm⁻², as expected from the enhanced hydrophobicity, while the electric outputs of the flat TENGs showed a dramatic decrease to 14 V and 8 μA cm⁻², respectively, corresponding to only 18% of the initial voltage value, due to dissipations of charges by water layer formation (Fig. 17a and b).

Furthermore, electrical outputs could be improved further by increasing the hydrophobicity of LbL-TENGs by treating the hierarchical PDMS surfaces with 1H, 1H, 2H, 2H-perfluorooctyltrichlorosilane (FOTS) [141,142]. Along with the high electron affinity of fluorine, the low surface energy of FOTS can have advantages in terms of increasing the hydrophobicity. In contrast to the untreated dual-sized PDMS film, the water contact angle on the fluorinated PDMS surface was 147°, which is close to superhydrophobic (Fig. 17d). After the formation of an SAM with FOTS on the LbL-induced dual-sized PDMS film, the electric outputs of the LbL-TENGs, as measured by the open-circuit voltage and short-circuit current density, were increased to 288 V and 17 μA cm⁻², respectively. In addition, a power density of 18.5 W m⁻² was measured by applying an external load resistance from 10³ to 10⁹ Ω, with the fluorinated LbL-TENGs (Fig. 17e). The electrical output performance of the fluorinated LbL-TENG in 80% RH conditions was decreased by approximately only 16%, corresponding to an output voltage of 242 V and a current density of 14.2 μA cm⁻² (Fig. 17f).

5. Summary and perspective

This review summarized recent research trends for piezoelectric NGs and

triboelectric devices using LbL assembly approaches based on covalent bonding and weak electrostatic interactions. The major advantages and characteristics of LbL assembly for the preparation of energy-harvesting films were systematically investigated from the viewpoints of the LbL-assembled components, adsorption mechanism, interfacial interactions, loading amount of electrically active components, surface morphology control, and device performance improvement.

First, most solution-processable piezoelectric nanocomposite films reported to date have been prepared using a simple blending process between perovskite-type ferroelectric nanomaterials with bulky size (> 200 nm) and polymers, generally restricting the development of ultrathin PENGs. On the other hand, the traditional electrostatic LbL assembly performed in aqueous media is also inappropriate for the preparation of such capacitor-type films with MIM structure because of the evolution of undesirable leakage current by residual moisture in addition to the low loading number of inorganic NPs occurring from electrostatic repulsion between same-charge NPs. As an alternative, it has been demonstrated that oleic acid-stabilized BTO NPs with sizes of 8–13 nm can be directly LbL-assembled with NH₂- or COOH-functionalized polymers through a unique ligand-addition mechanism in organic media. The piezoelectric performance of the formed ultrathin nanocomposite films can be precisely and easily controlled by the bilayer number under external compressive force. Furthermore, considering that a variety of perovskite-type ferroelectric NPs can be synthesized using various fatty acid ligands including oleic acid in organic media, we envision that ultrathin piezoelectric NGs with higher piezoelectric performance and additional integrated functionalities can be prepared using the ligand-addition LbL assembly approach.

Furthermore, it has been demonstrated that electrostatic LbL assembly can be effectively applied to the fabrication of triboelectric PDMS films with hierarchical surface morphology or dual-size surface structures. Subsequent PDMS replicas using (1) multicolloidal films (i.e., the anionic 0.6 μm-sized PS colloid/cationic polyelectrolyte/2 μm-sized PS colloid/substrate) or (2) acid treatment-induced porous PAH/PAA multilayers were used to generate triboelectric PDMS films with micro- and nanosized PDMS protruberances, which significantly increased the charge generation area and structure-induced hydrophobicity. As a result, these TENG devices based on the dual-size structured PDMS displayed much higher output voltage and current density than flat PDMS-based TENG devices in various humidity conditions. LbL-assembled films have previously been used as a mold for the preparation of PDMS replicas, the relatively new application of LbL assembly to triboelectric metal electrodes with positive polarity can open up the way for further increasing triboelectric performance due to the formation of larger charge generation areas. To this end, more systematic studies must focus on the interfacial interactions between the triboelectric metal electrode and metal NPs. Furthermore, if PDMS-based Al or Au electrodes with high flexibility and compressibility can be developed using LbL assembly, then we suggest that the electrical performance of TENGs can be significantly enhanced over that of various TENGs reported to date.

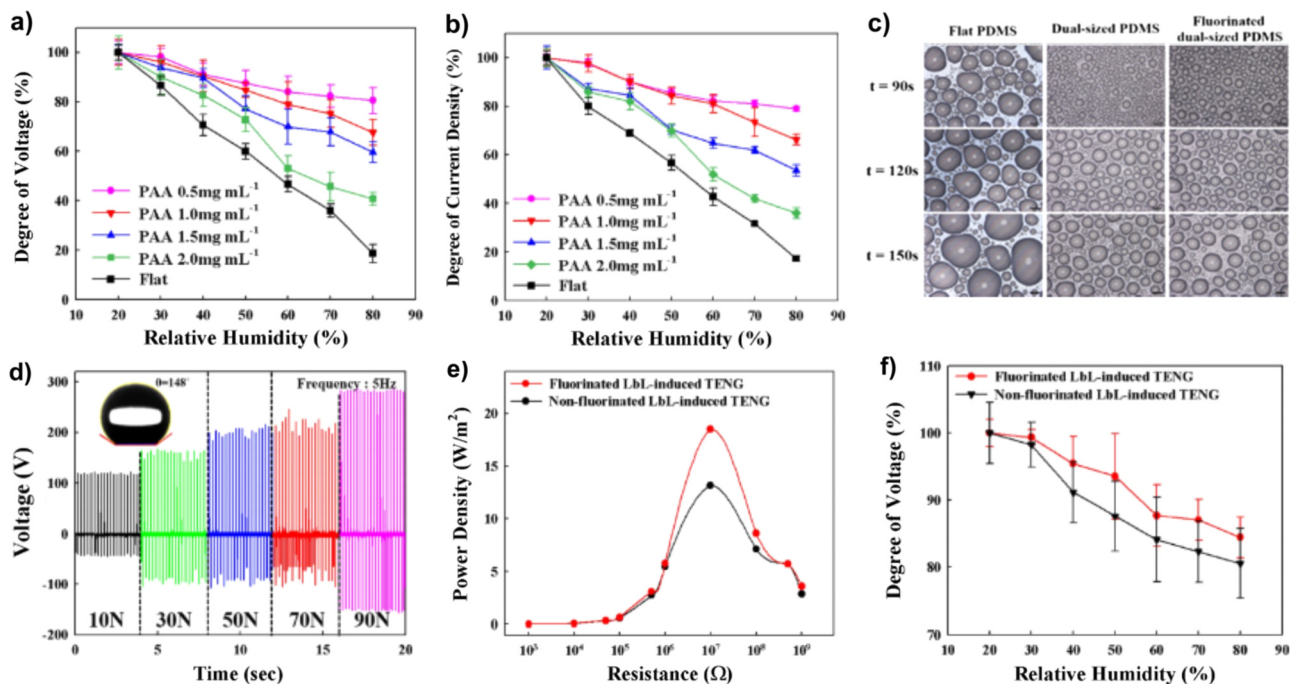


Fig. 17. The degree of the (a) output voltages and (b) current densities for the flat PDMS, 26 and four different LbL-TENGs as a function of the RH. (c) Condensation states of flat PDMS, dual structure-sized embossed PDMS and fluorinated dual structure-sized PDMS replicas under excess saturated vapor condition. (d) Voltage output of LbL-TENG composed of fluorinated [1.5 mg mL^{-1} PAH/ 0.5 mg mL^{-1} PAA]₂₀-induced PDMS replica and Al electrode. (e) Dependences of the power densities of fluorinated and non-fluorinated LbL-TENGs on the external load resistance. (f) Degree of voltages of fluorinated and non-fluorinated LbL-TENGs as a function of RH. In this case, the PDMS plates used for fluorinated and non-fluorinated LbL-TENGs were replicated from [1.5 mg mL^{-1} PAH/ 0.5 mg mL^{-1} PAA]₂₀ films [140]. Reproduced with permission from Elsevier B.V (2018).

Acknowledgements

This work was supported by the National Research Foundation (NRF) grant funded by the Korean government (2018R1A2A1A05019452; 2018R1C1B6008411). This work was also supported by the DGIST R&D Programs of Ministry of Science, ICT and Future Planning of Republic of Korea (18-ET-01). We thank our group members (Dongjin Jang, Dojin Kim, and Yongmin Ko) and collaborators (Prof. Sang-Woo Kim and Prof. Yonng Jeong) for their contributions to the work reviewed here.

Appendix A. Supporting information

Supplementary data associated with this article can be found in the online version at [doi:10.1016/j.nanoen.2018.11.024](https://doi.org/10.1016/j.nanoen.2018.11.024).

References

- G. Decher, J.-D. Hong, Buildup of ultrathin multilayer films by a self-assembly process, 1 consecutive adsorption of anionic and cationic bipolar amphiphiles on charged surfaces, *Macromol. Symp.* 46 (1) (1991) 321–327, <https://doi.org/10.1002/masy.19910460145>.
- G. Decher, J.D. Hong, J. Schmitt, Buildup of ultrathin multilayer films by a self-assembly process: III. Consecutively alternating adsorption of anionic and cationic polyelectrolytes on charged surfaces, *Thin Solid Films* 210–211 (1992) 831–835, [https://doi.org/10.1016/0040-6090\(92\)90417-a](https://doi.org/10.1016/0040-6090(92)90417-a).
- G. Decher, Fuzzy nanoassemblies: toward layered polymeric multicomposites, *Science* 277 (5330) (1997) 1232, <https://doi.org/10.1126/science.277.5330.1232>.
- F. Caruso, R.A. Caruso, H. Möhwald, Nanoengineering of inorganic and hybrid hollow spheres by colloidal templating, *Science* 282 (5391) (1998) 1111, <https://doi.org/10.1126/science.282.5391.1111>.
- T. Cassagneau, T.E. Mallouk, J.H. Fendler, Layer-by-layer assembly of thin film zener diodes from conducting polymers and CdSe nanoparticles, *J. Am. Chem. Soc.* 120 (31) (1998) 7848–7859, <https://doi.org/10.1021/ja9806027>.
- S.S. Shiratori, M.F. Rubner, pH-Dependent thickness behavior of sequentially adsorbed layers of weak polyelectrolytes, *Macromolecules* 33 (11) (2000) 4213–4219, <https://doi.org/10.1021/ma991645q>.
- J. Cho, K. Char, J.D. Hong, K.B. Lee, Fabrication of highly ordered multilayer films using a spin self-assembly method, *Adv. Mater.* 13 (14) (2001) 1076–1078, [https://doi.org/10.1002/1521-4095\(200107\)13:14<1076::aid-adma1076>3.0.co;2-m](https://doi.org/10.1002/1521-4095(200107)13:14<1076::aid-adma1076>3.0.co;2-m).
- S.T. Dubas, T.R. Farhat, J.B. Schlenoff, Multiple membranes from “True” polyelectrolyte multilayers, *J. Am. Chem. Soc.* 123 (22) (2001) 5368–5369, <https://doi.org/10.1021/ja015774>.
- H. Ai, M. Fang, S.A. Jones, Y.M. Lvov, Electrostatic layer-by-layer nanoassembly on biological microtemplates: platelets, *Biomacromolecules* 3 (3) (2002) 560–564, <https://doi.org/10.1021/bm015659r>.
- J.A. Hiller, J.D. Mendelsohn, M.F. Rubner, Reversibly erasable nanoporous anti-reflection coatings from polyelectrolyte multilayers, *Nat. Mater.* 1 (2002) 59, <https://doi.org/10.1038/nmat719>.
- Z. Tang, N.A. Kotov, S. Magonov, B. Ozturk, Nanostructured artificial nacre, *Nat. Mater.* 2 (2003) 413, <https://doi.org/10.1038/nmat906>.
- L. Zhai, A.J. Nolte, R.E. Cohen, M.F. Rubner, pH-Gated porosity transitions of polyelectrolyte multilayers in confined geometries and their application as tunable Bragg reflectors, *Macromolecules* 37 (16) (2004) 6113–6123, <https://doi.org/10.1021/ma049593e>.
- C. Jiang, S. Markutsya, Y. Pikus, V.V. Tsukruk, Freely suspended nanocomposite membranes as highly sensitive sensors, *Nat. Mater.* 3 (2004) 721, <https://doi.org/10.1038/nmat1212>.
- J. Cho, K. Char, Effect of layer integrity of spin self-assembled multilayer films on surface wettability, *Langmuir* 20 (10) (2004) 4011–4016, <https://doi.org/10.1021/la035476l>.
- J. Cho, J.F. Quinn, F. Caruso, Fabrication of polyelectrolyte multilayer films comprising nanoblended layers, *J. Am. Chem. Soc.* 126 (8) (2004) 2270–2271, <https://doi.org/10.1021/ja039830d>.
- Y. Wang, A. Yu, F. Caruso, Nanoporous polyelectrolyte spheres prepared by sequentially coating sacrificial mesoporous silica spheres, *Angew. Chem. Int. Ed.* 44 (19) (2005) 2888–2892, <https://doi.org/10.1002/anie.200462135>.
- J. Cho, J. Hong, K. Char, F. Caruso, Nanoporous block copolymer micelle/micelle multilayer films with dual optical properties, *J. Am. Chem. Soc.* 128 (30) (2006) 9935–9942, <https://doi.org/10.1021/ja062437y>.
- J.-S. Lee, J. Cho, C. Lee, I. Kim, J. Park, Y.-M. Kim, H. Shin, J. Lee, F. Caruso, Layer-by-layer assembled charge-trap memory devices with adjustable electronic properties, *Nat. Nanotechnol.* 2 (2007) 790, <https://doi.org/10.1038/nano.2007.380>.
- J. Hong, W.K. Bae, H. Lee, S. Oh, K. Char, F. Caruso, J. Cho, Tunable superhydrophobic and optical properties of colloidal films coated with block-copolymer-micelles/micelle-multilayers, *Adv. Mater.* 19 (24) (2007) 4364–4369, <https://doi.org/10.1002/adma.200701362>.
- J. Park, I. Kim, H. Shin, M.J. Lee, Y.S. Kim, J. Bang, F. Caruso, J. Cho, Integrated catalytic activity of patterned multilayer films based on pH-induced electrostatic properties of enzymes, *Adv. Mater.* 20 (10) (2008) 1843–1848, <https://doi.org/10.1002/adma.200702407>.
- D. Zimnitsky, V.V. Shevchenko, V.V. Tsukruk, Perforated, freely suspended layer-by-layer nanoscale membranes, *Langmuir* 24 (12) (2008) 5996–6006, <https://doi.org/10.1021/la7038575>.
- S. Lee, B. Lee, B.J. Kim, J. Park, M. Yoo, W.K. Bae, K. Char, C.J. Hawker, J. Bang, J. Cho, Free-standing nanocomposite multilayers with various length scales, adjustable internal structures, and functionalities, *J. Am. Chem. Soc.* 131 (7) (2009) 2579–2587, <https://doi.org/10.1021/ja8064478>.
- B. Lee, Y. Kim, S. Lee, Y.S. Kim, D. Wang, J. Cho, layer-by-layer growth of polymer/quantum dot composite multilayers by nucleophilic substitution in organic media, *Angew. Chem. Int. Ed.* 49 (2) (2009) 359–363, <https://doi.org/10.1002/anie.200905596>.
- W.K. Bae, J. Kwak, J. Lim, D. Lee, M.K. Nam, K. Char, C. Lee, S. Lee, Multicolored light-emitting diodes based on all-quantum-dot multilayer films using layer-by-layer assembly method, *Nano Lett.* 10 (7) (2010) 2368–2373, <https://doi.org/10.1021/nl100168s>.
- Y. Kim, C. Lee, I. Shim, D. Wang, J. Cho, Nucleophilic substitution reaction based layer-by-layer growth of superparamagnetic nanocomposite films with high nonvolatile memory performance, *Adv. Mater.* 22 (45) (2010) 5140–5144, <https://doi.org/10.1002/adma.201002142>.
- S.W. Lee, J. Kim, S. Chen, P.T. Hammond, Y. Shao-Horn, Carbon nanotube/manganese oxide ultrathin film electrodes for electrochemical capacitors, *ACS Nano* 4 (7) (2010) 3889–3896, <https://doi.org/10.1021/nn100681d>.
- Y. Ko, Y. Kim, H. Baek, J. Cho, Electrically bistable properties of layer-by-layer assembled multilayers based on protein nanoparticles, *ACS Nano* 5 (12) (2011) 9918–9926, <https://doi.org/10.1021/nn2036939>.

- [28] C.A. Nguyen, A.A. Argun, P.T. Hammond, X. Lu, P.S. Lee, Layer-by-layer assembled solid polymer electrolyte for electrochromic devices, *Chem. Mater.* 23 (8) (2011) 2142–2149, <https://doi.org/10.1021/cm103572q>.
- [29] M.N. Hyder, B.M. Gallant, N.J. Shah, Y. Shao-Horn, P.T. Hammond, Synthesis of highly stable sub-8 nm TiO₂ nanoparticles and their multilayer electrodes of TiO₂/MWNT for electrochemical applications, *Nano Lett.* 13 (10) (2013) 4610–4619, <https://doi.org/10.1021/nl401387s>.
- [30] Y. Ko, H. Baek, Y. Kim, M. Yoon, J. Cho, Hydrophobic nanoparticle-based nanocomposite films using in situ ligand exchange layer-by-layer assembly and their non-volatile memory applications, *ACS Nano* 7 (1) (2013) 143–153, <https://doi.org/10.1021/nn3034524>.
- [31] M. Park, Y. Kim, Y. Ko, S. Cheong, S.W. Ryu, J. Cho, Amphiphilic layer-by-layer assembly overcoming solvent polarity between aqueous and nonpolar media, *J. Am. Chem. Soc.* 136 (49) (2014) 17213–17223, <https://doi.org/10.1021/ja509168g>.
- [32] Y. Ko, D. Shin, B. Koo, S. Woo Lee, W.-S. Yoon, J. Cho, Ultrathin supercapacitor electrodes with high volumetric capacitance and stability using direct covalent-bonding between pseudocapacitive nanoparticles and conducting materials, *Nano Energy* 12 (2015) 612–625, <https://doi.org/10.1016/j.nanoen.2015.01.002>.
- [33] T. Lee, S.H. Min, M. Gu, Y.K. Jung, W. Lee, J.U. Lee, D.G. Seong, B.-S. Kim, Layer-by-layer assembly for graphene-based multilayer nanocomposites: synthesis and applications, *Chem. Mater.* 27 (11) (2015) 3785–3796, <https://doi.org/10.1021/acs.chemmater.5b00491>.
- [34] J. Cui, J.J. Richardson, M. Björnalm, M. Faria, F. Caruso, Nanoengineered templated polymer particles: navigating the biological realm, *Acc. Chem. Res.* 49 (6) (2016) 1139–1148, <https://doi.org/10.1021/acs.accounts.6b00088>.
- [35] I. Cho, H. Jung, B.G. Jeong, J.H. Chang, Y. Kim, K. Char, D.C. Lee, C. Lee, J. Cho, W.K. Bae, Multifunctional dendrimer ligands for high-efficiency, solution-processed quantum dot light-emitting diodes, *ACS Nano* 11 (1) (2017) 684–692, <https://doi.org/10.1021/acsnano.6b07028>.
- [36] Y. Ko, M. Kwon, W.K. Bae, B. Lee, S.W. Lee, J. Cho, Flexible supercapacitor electrodes based on real metal-like cellulose papers, *Nat. Commun.* 8 (1) (2017) 536, <https://doi.org/10.1038/s41467-017-00550-3>.
- [37] J.D. Mendelsohn, C.J. Barrett, V.V. Chan, A.J. Pal, A.M. Mayes, M.F. Rubner, Fabrication of microporous thin films from polyelectrolyte multilayers, *Langmuir* 16 (11) (2000) 5017–5023, <https://doi.org/10.1021/la00075g>.
- [38] J. Choi, M.F. Rubner, Influence of the degree of ionization on weak polyelectrolyte multilayer assembly, *Macromolecules* 38 (1) (2005) 116–124, <https://doi.org/10.1021/ma048596o>.
- [39] K.C. Grabar, K.J. Allison, B.E. Baker, R.M. Bright, K.R. Brown, R.G. Freeman, A.P. Fox, C.D. Keating, M.D. Musick, M.J. Natan, Two-dimensional arrays of colloidal gold particles: a flexible approach to macroscopic metal surfaces, *Langmuir* 12 (10) (1996) 2353–2361, <https://doi.org/10.1021/la950561h>.
- [40] J. Schmitt, G. Decher, W.J. Dressick, S.L. Brandow, R.E. Geer, R. Shashidhar, J.M. Calvert, Metal nanoparticle/polymer superlattice films: fabrication and control of layer structure, *Adv. Mater.* 9 (1) (1997) 61–65, <https://doi.org/10.1002/adma.1997090911>.
- [41] K.E. Tettery, M.Q. Yee, D. Lee, Layer-by-layer assembly of charged particles in nonpolar media, *Langmuir* 26 (12) (2010) 9974–9980, <https://doi.org/10.1021/la1000655>.
- [42] H.-C. Huang, N.S. Zacharia, Polyelectrolyte multilayers and complexes to modify secondary interactions in ethylene-co-methacrylic acid ionomers, *ACS Macro Lett.* 1 (1) (2012) 209–212, <https://doi.org/10.1021/mz200119b>.
- [43] M. Yoon, Y. Kim, J. Cho, Multifunctional colloids with optical, magnetic, and superhydrophobic properties derived from nucleophilic substitution-induced layer-by-layer assembly in organic media, *ACS Nano* 5 (7) (2011) 5417–5426, <https://doi.org/10.1021/nn200538a>.
- [44] Y. Kim, K. Kook, S.K. Hwang, C. Park, J. Cho, Polymer/perovskite-type nanoparticle multilayers with multielectric properties prepared from ligand addition-induced layer-by-layer assembly, *ACS Nano* 8 (3) (2014) 2419–2430, <https://doi.org/10.1021/nn405988d>.
- [45] Y. Kim, K.Y. Lee, S.K. Hwang, C. Park, S.-W. Kim, J. Cho, Layer-by-layer controlled perovskite nanocomposite thin films for piezoelectric nanogenerators, *Adv. Funct. Mater.* 24 (40) (2014) 6262–6269, <https://doi.org/10.1002/adfm.201401599>.
- [46] K.I. Park, M. Lee, Y. Liu, S. Moon, G.T. Hwang, G. Zhu, J.E. Kim, S.O. Kim, D.K. Kim, Z.L. Wang, K.J. Lee, Flexible nanocomposite generator made of BaTiO₃ nanoparticles and graphitic carbons (2937), *Adv. Mater.* 24 (22) (2012) 2999–3004, <https://doi.org/10.1002/adma.201290128>.
- [47] S.-H. Shin, Y.-H. Kim, M.H. Lee, J.-Y. Jung, J. Nah, Hemispherically aggregated BaTiO₃ nanoparticle composite thin film for high-performance flexible piezoelectric nanogenerator, *ACS Nano* 8 (3) (2014) 2766–2773, <https://doi.org/10.1021/nn406481k>.
- [48] Y. Zhao, Q. Liao, G. Zhang, Z. Zhang, Q. Liang, X. Liao, Y. Zhang, High output piezoelectric nanocomposite generators composed of oriented BaTiO₃ NPs@PVDF, *Nano Energy* 11 (2015) 719–727, <https://doi.org/10.1016/j.nanoen.2014.11.061>.
- [49] X. Chen, X. Li, J. Shao, N. An, H. Tian, C. Wang, T. Han, L. Wang, B. Lu, High-performance piezoelectric nanogenerators with imprinted P(VDF-TrFE)/BaTiO₃ nanocomposite micropillars for self-powered flexible sensors, *Small* 13 (23) (2017), <https://doi.org/10.1002/sml.201604245>.
- [50] P.G. Kang, T.K. Lee, C.W. Ahn, I.W. Kim, H.H. Lee, S.B. Choi, K.D. Sung, J.H. Jung, Vertically aligned epitaxial KNbO₃ nanorod array for piezoelectric energy harvester and second harmonic generator, *Nano Energy* 17 (2015) 261–268, <https://doi.org/10.1016/j.nanoen.2015.09.004>.
- [51] M.-R. Joung, H. Xu, I.-T. Seo, D.-H. Kim, J. Hur, S. Nahm, C.-Y. Kang, S.-J. Yoon, H.-M. Park, Piezoelectric nanogenerators synthesized using KNbO₃ nanowires with various crystal structures, *J. Mater. Chem. A* 2 (43) (2014) 18547–18553, <https://doi.org/10.1039/c4ta03551h>.
- [52] J.M. Wu, C. Xu, Y. Zhang, Z.L. Wang, Lead-free nanogenerator made from single ZnSnO₃ microbelt, *ACS Nano* 6 (5) (2012) 4335–4340, <https://doi.org/10.1021/nn300951d>.
- [53] K.Y. Lee, D. Kim, J.-H. Lee, T.Y. Kim, M.K. Gupta, S.-W. Kim, Unidirectional high-power generation via stress-induced dipole alignment from ZnSnO₃ nanocubes/polymer hybrid piezoelectric nanogenerator, *Adv. Funct. Mater.* 24 (1) (2014) 37–43, <https://doi.org/10.1002/adfm.201301379>.
- [54] M.J. Polking, M.G. Han, A. Yourdkhani, V. Petkov, C.F. Kisielowski, V.V. Volkov, Y. Zhu, G. Caruntu, A.P. Alivisatos, R. Ramesh, Ferroelectric order in individual nanometre-scale crystals, *Nat. Mater.* 11 (8) (2012) 700–709, <https://doi.org/10.1038/nmat3371>.
- [55] P. Martins, A.C. Lopes, S. Lanceros-Mendez, Electroactive phases of poly(vinylidene fluoride): determination, processing and applications, *Prog. Polym. Sci.* 39 (4) (2014) 683–706, <https://doi.org/10.1016/j.poly.2013.07.006>.
- [56] L. Zhu, Q. Wang, Novel ferroelectric polymers for high energy density and low loss dielectrics, *Macromolecules* 45 (7) (2012) 2937–2954, <https://doi.org/10.1021/ma2024057>.
- [57] P. Uebberschlag, PVDF piezoelectric polymer, *Sens. Rev.* 21 (2) (2001) 118–126, <https://doi.org/10.1108/02602280110388315>.
- [58] W. Ma, J. Zhang, S. Chen, X. Wang, Crystalline phase formation of poly(vinylidene fluoride) from tetrahydrofuran/*N,N*-dimethylformamide mixed solutions, *J. Macromol. Sci. B* 47 (3) (2008) 434–449, <https://doi.org/10.1080/0022340801954811>.
- [59] Prateek, V.K. Thakur, R.K. Gupta, Recent progress on ferroelectric polymer-based nanocomposites for high energy density capacitors: synthesis, dielectric properties, and future aspects, *Chem. Rev.* 116 (7) (2016) 4260–4317, <https://doi.org/10.1021/acs.chemrev.5b00495>.
- [60] M.K. Corbierre, N.S. Cameron, M. Sutton, S.G.J. Mochrie, L.B. Lurio, A. Rühm, R.B. Lennox, Polymer-stabilized gold nanoparticles and their incorporation into polymer matrices, *J. Am. Chem. Soc.* 123 (42) (2001) 10411–10412, <https://doi.org/10.1021/ja0166287>.
- [61] M. Okuyama, Y. Hamakawa, Preparation and basic properties of PbTiO₃ ferroelectric thin films and their device applications, *Ferroelectrics* 63 (1) (1985) 243–252, <https://doi.org/10.1080/00150198508221406>.
- [62] N.A. Pertsev, A.K. Tagantsev, N. Setter, Phase transitions and strain-induced ferroelectricity in SrTiO₃ epitaxial thin films, *Phys. Rev. B* 61 (2) (2000) R825–R829, <https://doi.org/10.1103/PhysRevB.61.R825>.
- [63] K.J. Choi, M. Biogalski, Y.L. Li, A. Sharan, J. Schubert, R. Uecker, P. Reiche, Y.B. Chen, X.Q. Pan, V. Gopalan, L.Q. Chen, D.G. Schlom, C.B. Eom, Enhancement of ferroelectricity in strained BaTiO₃ thin films, *Science* 306 (5698) (2004) 1005, <https://doi.org/10.1126/science.1103218>.
- [64] C.-L. Jia, K.W. Urban, M. Alexe, D. Hesse, I. Vrejoiu, Direct observation of continuous electric dipole rotation in flux-closure domains in ferroelectric Pb(Zr,Ti)O₃, *Science* 331 (6023) (2011) 1420, <https://doi.org/10.1126/science.1206005>.
- [65] T. Kumazawa, Y. Kumagai, H. Miura, M. Kitano, K. Kushida, Effect of external stress on polarization in ferroelectric thin films, *Appl. Phys. Lett.* 72 (5) (1998) 608–610, <https://doi.org/10.1063/1.120820>.
- [66] A. Gruverman, B.J. Rodriguez, A.I. Kingon, R.J. Nemanich, A.K. Tagantsev, J.S. Cross, M. Tsukada, Mechanical stress effect on imprint behavior of integrated ferroelectric capacitors, *Appl. Phys. Lett.* 83 (4) (2003) 728–730, <https://doi.org/10.1063/1.1593830>.
- [67] S. Bai, Q. Xu, L. Gu, F. Ma, Y. Qin, Z.-L. Wang, Single crystalline lead zirconate titanate (PZT) nano/micro-wire based self-powered UV sensor, *Nano Energy* 1 (6) (2012) 789–795, <https://doi.org/10.1016/j.nanoen.2012.09.001>.
- [68] S. Siddiqui, D.-I. Kim, L.T. Duy, M.T. Nguyen, S. Muhammad, W.-S. Yoon, N.-E. Lee, High-performance flexible lead-free nanocomposite piezoelectric nanogenerator for biomechanical energy harvesting and storage, *Nano Energy* 15 (2015) 177–185, <https://doi.org/10.1016/j.nanoen.2015.04.030>.
- [69] K.N. Kim, J. Chun, S.A. Chae, C.W. Ahn, I.W. Kim, S.-W. Kim, Z.L. Wang, J.M. Baik, Silk fibroin-based biodegradable piezoelectric composite nanogenerators using lead-free ferroelectric nanoparticles, *Nano Energy* 14 (2015) 87–94, <https://doi.org/10.1016/j.nanoen.2015.01.004>.
- [70] K.I. Park, S. Xu, Y. Liu, G.T. Hwang, S.J. Kang, Z.L. Wang, K.J. Lee, Piezoelectric BaTiO₃ (3) thin film nanogenerator on plastic substrates, *Nano Lett.* 10 (12) (2010) 4939–4943, <https://doi.org/10.1021/nl102959k>.
- [71] Y.-Z. Chen, T.-H. Liu, C.-Y. Chen, C.-H. Liu, S.-Y. Chen, W.-W. Wu, Z.L. Wang, J.-H. He, Y.-H. Chu, Y.-L. Chueh, Taper PbZr_{0.2}Ti_{0.8}O₃ nanowire arrays: from controlled growth by pulsed laser deposition to piezopotential measurements, *ACS Nano* 6 (3) (2012) 2826–2832, <https://doi.org/10.1021/nn300370m>.
- [72] J.H. Jung, M. Lee, J.-I. Hong, Y. Ding, C.-Y. Chen, L.-J. Chou, Z.L. Wang, Lead-free NaNbO₃ nanowires for a high output piezoelectric nanogenerator, *ACS Nano* 5 (12) (2011) 10041–10046, <https://doi.org/10.1021/nn2039033>.
- [73] Z.H. Lin, Y. Yang, J.M. Wu, Y. Liu, F. Zhang, Z.L. Wang, BaTiO₃ nanotubes-based flexible and transparent nanogenerators, *J. Phys. Chem. Lett.* 3 (23) (2012) 3599–3604, <https://doi.org/10.1021/jz301805f>.
- [74] K.I. Park, J.H. Son, G.T. Hwang, C.K. Jeong, J. Ryu, M. Koo, I. Choi, S.H. Lee, M. Byun, Z.L. Wang, K.J. Lee, Highly-efficient, flexible piezoelectric PZT thin film nanogenerator on plastic substrates, *Adv. Mater.* 26 (16) (2014) 2514–2520, <https://doi.org/10.1002/adma.201305659>.
- [75] S. O'Brien, L. Brus, C.B. Murray, Synthesis of monodisperse nanoparticles of barium titanate: toward a generalized strategy of oxide nanoparticle synthesis, *J. Am. Chem. Soc.* 123 (48) (2001) 12085–12086, <https://doi.org/10.1021/ja011414a>.
- [76] X. Wang, J. Zhuang, Q. Peng, Y. Li, A general strategy for nanocrystal synthesis, *Nature* 437 (7055) (2005) 121–124, <https://doi.org/10.1038/nature03968>.
- [77] M. Niederberger, N. Pinna, J. Polleux, M. Antonietti, A general soft-chemistry route to perovskites and related materials: synthesis of BaTiO₃(3), BaZrO₃(3), and LiNbO₃(3) nanoparticles, *Angew. Chem. Int. Ed.* 43 (17) (2004) 2270–2273, <https://doi.org/10.1002/anie.200353300>.
- [78] M. Niederberger, G. Garnweitner, N. Pinna, M. Antonietti, Nonaqueous and halide-free route to crystalline BaTiO₃, SrTiO₃, and (Ba,Sr)TiO₃ nanoparticles via a mechanism involving C–C bond formation, *J. Am. Chem. Soc.* 126 (29) (2004) 9120–9126, <https://doi.org/10.1021/ja0494959>.
- [79] Z. Chen, L. Huang, J. He, Y. Zhu, S. O'Brien, New nonhydrolytic route to synthesize crystalline BaTiO₃ nanocrystals with surface capping ligands, *J. Mater. Res.* 21 (12) (2006) 3187–3195, <https://doi.org/10.1557/jmr.2006.0389>.
- [80] A.F. Demirörs, A. Imhof, BaTiO₃, SrTiO₃, CaTiO₃, and BaSr_{1-x}TiO₃Particles: a general approach for monodisperse colloidal perovskites, *Chem. Mater.* 21 (13) (2009) 3002–3007, <https://doi.org/10.1021/cm900693r>.
- [81] L. Huang, Z. Jia, I. Kymissis, S. O'Brien, HighCapacitors and OFET gate dielectrics from self-assembled BaTiO₃ and (Ba,Sr)TiO₃ nanocrystals in the superparaelectric limit, *Adv. Funct. Mater.* 20 (4) (2010) 554–560, <https://doi.org/10.1002/adfm.200901258>.
- [82] S. Adireddy, C. Lin, B. Cao, W. Zhou, G. Caruntu, Solution-based growth of monodisperse cube-like BaTiO₃ colloidal nanocrystals, *Chem. Mater.* 22 (6) (2010) 1946–1948, <https://doi.org/10.1021/cm903876f>.
- [83] F. Dang, K. Mimura, K. Kato, H. Imai, S. Wada, H. Haneda, M. Kuwabara, In situ growth BaTiO₃ nanocubes and their superlattice from an aqueous process, *Nanoscale* 4 (4) (2012) 1344–1349, <https://doi.org/10.1039/c2nr11594h>.
- [84] F. Dang, K.-i. Mimura, K. Kato, H. Imai, S. Wada, H. Haneda, M. Kuwabara, Growth of monodispersed SrTiO₃ nanocubes by thermohydrolysis method, *CrystEngComm* 13 (11) (2011), <https://doi.org/10.1039/c1ce05296a>.
- [85] K.-i. Mimura, K. Kato, H. Imai, S. Wada, H. Haneda, M. Kuwabara, Fabrication and characterization of dielectric nanocube self-assembled structures, *Jpn. J. Appl. Phys.* 51 (2012), <https://doi.org/10.7567/jjap.51.09l0c3>.
- [86] D. Caruntu, T. Rostamzadeh, T. Costanzo, S.E. Parizi, G. Caruntu, Solvothermal synthesis

- and controlled self-assembly of monodisperse titanium-based perovskite colloidal nanocrystals, *Nanoscale* 7 (30) (2015) 12955–12969, <https://doi.org/10.1039/c5nr00737b>.
- [87] M. Coll, A. Gomez, E. Mas-Marza, O. Almora, G. Garcia-Belmonte, M. Campoy-Quiles, J. Bisquert, Polarization switching and light-enhanced piezoelectricity in lead halide perovskites, *J. Phys. Chem. Lett.* 6 (8) (2015) 1408–1413, <https://doi.org/10.1021/acs.jpclett.5b00502>.
- [88] Y. Kawamura, H. Mashiyama, K. Hasebe, Structural study on cubic–tetragonal transition of CH₃NH₃PbI₃, *J. Phys. Soc. Jpn.* 71 (7) (2002) 1694–1697, <https://doi.org/10.1143/jpsj.71.1694>.
- [89] J.M. Frost, K.T. Butler, A. Walsh, Molecular ferroelectric contributions to anomalous hysteresis in hybrid perovskite solar cells, *APL Mater.* 2 (8) (2014), <https://doi.org/10.1063/1.4890246>.
- [90] Y.-J. Kim, T.-V. Dang, H.-J. Choi, B.-J. Park, J.-H. Eom, H.-A. Song, D. Seol, Y. Kim, S.-H. Shin, J. Nah, S.-G. Yoon, Piezoelectric properties of CH₃NH₃PbI₃ perovskite thin films and their applications in piezoelectric generators, *J. Mater. Chem. A* 4 (3) (2016) 756–763, <https://doi.org/10.1039/c5ta09662f>.
- [91] S. Ippili, V. Jella, J. Kim, S. Hong, S.-G. Yoon, Enhanced piezoelectric output performance via control of dielectrics in Fe²⁺-incorporated MAPbI₃ perovskite thin films: flexible piezoelectric generators, *Nano Energy* 49 (2018) 247–256, <https://doi.org/10.1016/j.nanoen.2018.04.031>.
- [92] R. Ding, H. Liu, X. Zhang, J. Xiao, R. Kishor, H. Sun, B. Zhu, G. Chen, F. Gao, X. Feng, J. Chen, X. Chen, X. Sun, Y. Zheng, Flexible piezoelectric nanocomposite generators based on formamidinium lead halide perovskite nanoparticles, *Adv. Funct. Mater.* 26 (42) (2016) 7708–7716, <https://doi.org/10.1002/adfm.201602634>.
- [93] R. Ding, X. Zhang, G. Chen, H. Wang, R. Kishor, J. Xiao, F. Gao, K. Zeng, X. Chen, X.W. Sun, Y. Zheng, High-performance piezoelectric nanogenerators composed of formamidinium lead halide perovskite nanoparticles and poly(vinylidene fluoride), *Nano Energy* 37 (2017) 126–135, <https://doi.org/10.1016/j.nanoen.2017.05.010>.
- [94] P. Kim, N.M. Doss, J.P. Tillotson, P.J. Hotchkiss, M.-J. Pan, S.R. Marder, J. Li, J.P. Calame, J.W. Perry, High energy density nanocomposites based on surface-modified BaTiO₃ and a ferroelectric polymer, *ACS Nano* 3 (9) (2009) 2581–2592, <https://doi.org/10.1021/nn9006412>.
- [95] X. Zhang, S. Wei, N. Haldolaarachchige, H.A. Colorado, Z. Luo, D.P. Young, Z. Guo, Magnetoresistive conductive polyaniline–barium titanate nanocomposites with negative permittivity, *J. Phys. Chem. C* 116 (29) (2012) 15731–15740, <https://doi.org/10.1021/jp303226u>.
- [96] D. Buttry, *Advances in electroanalytical chemistry: applications of the QCM to electrochemistry*, Marcel Dekker, New York, 1991.
- [97] F.R. Fan, Z.Q. Tian, Z.L. Wang, Flexible triboelectric generator!, *Nano Energy* 1 (2) (2012) 328–334, <https://doi.org/10.1016/j.nanoen.2012.01.004>.
- [98] G. Zhu, C. Pan, W. Guo, C.Y. Chen, Y. Zhou, R. Yu, Z.L. Wang, Triboelectric-generator-driven pulse electrodeposition for micropatterning, *Nano Lett.* 12 (9) (2012) 4960–4965, <https://doi.org/10.1021/nl302560k>.
- [99] C.K. Jeong, K.M. Baek, S. Niu, T.W. Nam, Y.H. Hur, D.Y. Park, G.T. Hwang, M. Byun, Z.L. Wang, Y.S. Jung, K.J. Lee, Topographically-designed triboelectric nanogenerator via block copolymer self-assembly, *Nano Lett.* 14 (12) (2014) 7031–7038, <https://doi.org/10.1021/nl503402c>.
- [100] S. Wang, Y. Xie, S. Niu, L. Lin, Z.L. Wang, Freestanding triboelectric-layer-based nanogenerators for harvesting energy from a moving object or human motion in contact and non-contact modes, *Adv. Mater.* 26 (18) (2014) 2818–2824, <https://doi.org/10.1002/adma.201305303>.
- [101] S. Kim, M.K. Gupta, K.Y. Lee, A. Sohn, T.Y. Kim, K.S. Shin, D. Kim, S.K. Kim, K.H. Lee, H.J. Shin, D.W. Kim, S.W. Kim, Transparent flexible graphene triboelectric nanogenerators, *Adv. Mater.* 26 (23) (2014) 3918–3925, <https://doi.org/10.1002/adma.201401172>.
- [102] K.Y. Lee, J. Chun, J.H. Lee, K.N. Kim, N.R. Kang, J.Y. Kim, M.H. Kim, K.S. Shin, M.K. Gupta, J.M. Baik, S.W. Kim, Hydrophobic sponge structure-based triboelectric nanogenerator, *Adv. Mater.* 26 (29) (2014) 5037–5042, <https://doi.org/10.1002/adma.201401184>.
- [103] L.B. Huang, W. Xu, G.X. Bai, M.C. Wong, Z.B. Yang, J.H. Hao, Wind energy and blue energy harvesting based on magnetic-assisted noncontact triboelectric nanogenerator, *Nano Energy* 30 (2016) 36–42, <https://doi.org/10.1016/j.nanoen.2016.09.032>.
- [104] L.B. Huang, G. Bai, M.C. Wong, Z. Yang, W. Xu, J. Hao, Magnetic-assisted noncontact triboelectric nanogenerator converting mechanical energy into electricity and light emissions, *Adv. Mater.* 28 (14) (2016) 2744–2751, <https://doi.org/10.1002/adma.201505839>.
- [105] L.B. Huang, W. Xu, J. Hao, Energy device applications of synthesized 1D polymer nanomaterials, *Small* 13 (43) (2017), <https://doi.org/10.1002/sml.201701820>.
- [106] Y. Guo, K. Li, C. Hou, Y. Li, Q. Zhang, H. Wang, Fluoroalkylsilane-modified textile-based personal energy management device for multifunctional wearable applications, *ACS Appl. Mater. Interfaces* 8 (7) (2016) 4676–4683, <https://doi.org/10.1021/acsami.5b11622>.
- [107] J. Xiong, M.-F. Lin, J. Wang, S.L. Gaw, K. Parida, P.S. Lee, Wearable all-fabric-based triboelectric generator for water energy harvesting, *Adv. Energy Mater.* 7 (21) (2017), <https://doi.org/10.1002/aenm.201701243>.
- [108] M.-O. Kim, S. Pyo, G. Song, W. Kim, Y. Oh, C. Park, J. Kim, Humidity-resistant, fabric-based, wearable triboelectric energy harvester by treatment of hydrophobic self-assembled monolayers, *Adv. Mater. Technol.* 3 (7) (2018) 1800048, <https://doi.org/10.1002/admt.201800048>.
- [109] J.-N. Wang, Y.-Q. Liu, Y.-L. Zhang, J. Feng, H. Wang, Y.-H. Yu, H.-B. Sun, Wearable superhydrophobic elastomer skin with switchable wettability, *Adv. Funct. Mater.* 28 (23) (2018), <https://doi.org/10.1002/adfm.201800625>.
- [110] J. Chun, B.U. Ye, J.W. Lee, D. Choi, C.Y. Kang, S.W. Kim, Z.L. Wang, J.M. Baik, Boosted output performance of triboelectric nanogenerator via electric double layer effect, *Nat. Commun.* 7 (2016) 12985, <https://doi.org/10.1038/ncomms12985>.
- [111] V. Nguyen, R. Yang, Effect of humidity and pressure on the triboelectric nanogenerator, *Nano Energy* 2 (5) (2013) 604–608, <https://doi.org/10.1016/j.nanoen.2013.07.012>.
- [112] V. Nguyen, R. Zhu, R. Yang, Environmental effects on nanogenerators, *Nano Energy* 14 (2015) 49–61, <https://doi.org/10.1016/j.nanoen.2014.11.049>.
- [113] K. Liu, X. Yao, L. Jiang, Recent developments in bio-inspired special wettability, *Chem. Soc. Rev.* 39 (8) (2010) 3240–3255, <https://doi.org/10.1039/b917112f>.
- [114] K. Liu, L. Jiang, Bio-inspired design of multiscale structures for function integration, *Nano Today* 6 (2) (2011) 155–175, <https://doi.org/10.1016/j.nantod.2011.02.002>.
- [115] N. Miljkovic, R. Enright, E.N. Wang, Effect of droplet morphology on growth dynamics and heat transfer during condensation on superhydrophobic nanostructured surfaces, *ACS Nano* 6 (2) (2012) 1776–1785, <https://doi.org/10.1021/nn2050552a>.
- [116] L. Zheng, Z.-H. Lin, G. Cheng, W. Wu, X. Wen, S. Lee, Z.L. Wang, Silicon-based hybrid cell for harvesting solar energy and raindrop electrostatic energy, *Nano Energy* 9 (2014) 291–300, <https://doi.org/10.1016/j.nanoen.2014.07.024>.
- [117] G. Zhu, Y. Su, P. Bai, J. Chen, Q. Jing, W. Yang, Z.L. Wang, Harvesting water wave energy by asymmetric screening of electrostatic charges on a nanostructured hydrophobic thin-film surface, *ACS Nano* 8 (6) (2014) 6031–6037, <https://doi.org/10.1021/nn5012732>.
- [118] B. Dudem, Y.H. Ko, J.W. Leem, S.H. Lee, J.S. Yu, Highly transparent and flexible triboelectric nanogenerators with subwavelength-architected polydimethylsiloxane by a nanoporous anodic aluminum oxide template, *ACS Appl. Mater. Interfaces* 7 (37) (2015) 20520–20529, <https://doi.org/10.1021/acsami.5b05842>.
- [119] X. Li, M.-H. Yeh, Z.-H. Lin, H. Guo, P.-K. Yang, J. Wang, S. Wang, R. Yu, T. Zhang, Z.L. Wang, Self-powered triboelectric nanosensor for microfluidics and cavity-confined solution chemistry, *ACS Nano* 9 (11) (2015) 11056–11063, <https://doi.org/10.1021/acsnano.5b04486>.
- [120] Z.-H. Lin, G. Cheng, X. Li, P.K. Yang, X. Wen, Z. Lin Wang, A multi-layered interdigitated-electrodes-based triboelectric nanogenerator for harvesting hydropower, *Nano Energy* 15 (2015) 256–265, <https://doi.org/10.1016/j.nanoen.2015.04.037>.
- [121] Y. Feng, Y. Zheng, S. Ma, D. Wang, F. Zhou, W. Liu, High output polypropylene nanowire array triboelectric nanogenerator through surface structural control and chemical modification, *Nano Energy* 19 (2016) 48–57, <https://doi.org/10.1016/j.nanoen.2015.11.017>.
- [122] X. Yang, W.A. Daoud, Triboelectric and piezoelectric effects in a combined tribo-piezoelectric nanogenerator based on an interfacial ZnO nanostructure, *Adv. Funct. Mater.* 26 (45) (2016) 8194–8201, <https://doi.org/10.1002/adfm.201602529>.
- [123] A. Yu, X. Chen, H. Cui, L. Chen, J. Luo, W. Tang, M. Peng, Y. Zhang, J. Zhai, Z.L. Wang, Self-powered random number generator based on coupled triboelectric and electrostatic induction effects at the liquid-dielectric interface, *ACS Nano* 10 (12) (2016) 11434–11441, <https://doi.org/10.1021/acsnano.6b07030>.
- [124] L. Zhang, B. Zhang, J. Chen, L. Jin, W. Deng, J. Tang, H. Zhang, H. Pan, M. Zhu, W. Yang, Z.L. Wang, Lawn structured triboelectric nanogenerators for scavenging sweeping wind energy on rooftops, *Adv. Mater.* 28 (8) (2016) 1650–1656, <https://doi.org/10.1002/adma.201504462>.
- [125] X. Chen, Q. Xu, S. Bai, Y. Qin, A self-powered sensor with super-hydrophobic nanostructure surfaces for synchronous detection and electricity generation, *Nano Energy* 33 (2017) 288–292, <https://doi.org/10.1016/j.nanoen.2017.01.023>.
- [126] X.J. Zhao, S.Y. Kuang, Z.L. Wang, G. Zhu, Highly adaptive solid-liquid interfacial triboelectric nanogenerator for harvesting diverse water wave energy, *ACS Nano* 12 (5) (2018) 4280–4285, <https://doi.org/10.1021/acsnano.7b08716>.
- [127] D. Kim, S.-J. Park, S.-B. Jeon, M.-L. Seol, Y.-K. Choi, A triboelectric sponge fabricated from a cube sugar template by 3D soft lithography for superhydrophobicity and elasticity, *Adv. Electron. Mater.* 2 (4) (2016), <https://doi.org/10.1002/aelm.201500331>.
- [128] X. He, X. Mu, Q. Wen, Z. Wen, J. Yang, C. Hu, H. Shi, Flexible and transparent triboelectric nanogenerator based on high performance well-ordered porous PDMS dielectric film, *Nano Res.* 9 (12) (2016) 3714–3724, <https://doi.org/10.1007/s12274-016-1242-3>.
- [129] C. Cui, X. Wang, Z. Yi, B. Yang, X. Wang, X. Chen, J. Liu, C. Yang, Flexible single-electrode triboelectric nanogenerator and body moving sensor based on porous Na₂CO₃/polydimethylsiloxane film, *ACS Appl. Mater. Interfaces* 10 (4) (2018) 3652–3659, <https://doi.org/10.1021/acsami.7b17585>.
- [130] Z.-H. Lin, G. Cheng, W. Wu, K.C. Pradel, Z.L. Wang, Dual-mode triboelectric nanogenerator for harvesting water energy and as a self-powered Ethanol nanosensor, *ACS Nano* 8 (6) (2014) 6440–6448, <https://doi.org/10.1021/nn501983s>.
- [131] Z.H. Lin, G. Cheng, S. Lee, K.C. Pradel, Z.L. Wang, Harvesting water drop energy by a sequential contact-electrification and electrostatic-induction process, *Adv. Mater.* 26 (27) (2014) 4690–4696, <https://doi.org/10.1002/adma.201400373>.
- [132] B. Dudem, Y.H. Ko, J.W. Leem, J.H. Lim, J.S. Yu, Hybrid energy cell with hierarchical nano/micro-architected polymer film to harvest mechanical, solar, and wind energies individually/simultaneously, *ACS Appl. Mater. Interfaces* 8 (44) (2016) 30165–30175, <https://doi.org/10.1021/acsami.6b09785>.
- [133] M.L. Seol, J.H. Woo, D.I. Lee, H. Im, J. Hur, Y.K. Choi, Nature-replicated nano-in-micro structures for triboelectric energy harvesting, *Small* 10 (19) (2014) 3887–3894, <https://doi.org/10.1002/sml.201400863>.
- [134] S. Jin, Y. Wang, M. Motlag, S. Gao, J. Xu, Q. Nian, W. Wu, G.J. Cheng, Large-area direct laser-shock imprinting of a 3D biomimetic hierarchical metal surface for triboelectric nanogenerators, *Adv. Mater.* 30 (11) (2018), <https://doi.org/10.1002/adma.201705840>.
- [135] D. Choi, D.W. Kim, D. Yoo, K.J. Cha, M. La, D.S. Kim, Spontaneous occurrence of liquid-solid contact electrification in nature: toward a robust triboelectric nanogenerator inspired by the natural lotus leaf, *Nano Energy* 36 (2017) 250–259, <https://doi.org/10.1016/j.nanoen.2017.04.026>.
- [136] C. Park, T. Lee, Y. Xia, T.J. Shin, J. Myoung, U. Jeong, Quick, large-area assembly of a single-crystal monolayer of spherical particles by unidirectional rubbing, *Adv. Mater.* 26 (27) (2014) 4633–4638, <https://doi.org/10.1002/adma.201305875>.
- [137] C. Park, K. Koh, U. Jeong, Structural color painting by rubbing particle powder, *Sci. Rep.* 5 (2015) 8340, <https://doi.org/10.1038/srep08340>.
- [138] D. Jang, Y. Kim, T.Y. Kim, K. Koh, U. Jeong, J. Cho, Force-assembled triboelectric nanogenerator with high-humidity-resistant electricity generation using hierarchical surface morphology, *Nano Energy* 20 (2016) 283–293, <https://doi.org/10.1016/j.nanoen.2015.12.021>.
- [139] L. Zhai, F.C. Cebeci, R.E. Cohen, M.F. Rubner, Stable superhydrophobic coatings from polyelectrolyte multilayers, *Nano Lett.* 4 (7) (2004) 1349–1353, <https://doi.org/10.1021/nl049463j>.
- [140] D. Kim, S. Lee, Y. Ko, C.H. Kwon, J. Cho, Layer-by-layer assembly-induced triboelectric nanogenerators with high and stable electric outputs in humid environments, *Nano Energy* 44 (2018) 228–239, <https://doi.org/10.1016/j.nanoen.2017.12.001>.
- [141] G. Song, Y. Kim, S. Yu, M.-O. Kim, S.-H. Park, S.M. Cho, D.B. Velamamy, S.H. Cho, K.L. Kim, J. Kim, E. Kim, C. Park, Molecularly engineered surface triboelectric nanogenerator by self-assembled monolayers (MEMTS), *Chem. Mater.* 27 (13) (2015) 4749–4755, <https://doi.org/10.1021/acs.chemmater.5b01507>.
- [142] S.-H. Shin, Y.H. Kwon, Y.-H. Kim, J.-Y. Jung, M.H. Lee, J. Nah, Triboelectric charging sequence induced by surface functionalization as a method to fabricate high performance triboelectric generators, *ACS Nano* 9 (4) (2015) 4621–4627, <https://doi.org/10.1021/acsnano.5b01340>.